Journal of Biological Engineering

RESEARCH

Open Access

Enhancing in vitro osteogenic differentiation of mesenchymal stem cells via sustained dexamethasone delivery in 3D-Printed hybrid scaffolds based on polycaprolactone-nanohydroxyapatite/alginate-gelatin for bone regeneration

Parastoo Noory[1*], Ahmad Reza Farmani[2*], Jafar Ai[1*], Naghmeh Bahrami[1,3*], Mohammad Bayat[3], Somayeh Ebrahimi-Barough[1], Ali Farzin[4], Shima Shojaie[5], Hamed Hajmoradi[6], Abdolreza Mohamadnia[7,8] and Arash Goodarzi[2]

Abstract

Despite the natural ability of bone repair, its limitations have led to advanced organic-inorganic-based biomimetic scaffolds and sustained drug release approaches. Particularly, dexamethasone (DEX), a widely used synthetic glucocorticoid, has been shown to increase the expression of bone-related genes during the osteogenesis process. This study aims to develop a hybrid 3D-printed scaffold for controlled delivery of dexamethasone. Hence, hybrid scaffolds were fabricated using a layer-by-layer 3D-printing of combined materials comprising polycaprolactone (PCL)-nanohydroxyapatite (nHA) composite, and DEX-loaded PCL microparticles embedded in the alginate-gelatin hydrogel. Encapsulation efficiency, loading capacity, and in vitro kinetics of DEX release were evaluated. Osteogenic differentiation of human endometrial mesenchymal stem cells (hEnMSCs) on DEX-loaded hybrid scaffolds was assessed by evaluating osteogenic gene expression levels (collagen I, osteonectin, RUNX2), alkaline phosphatase (ALP) activity, and scaffold mineralization. The hybrid scaffolds exhibited favorable morphology, mechanical-properties, biocompatibility, and biodegradability, enhancing osteogenesis of hEnMSCs. DEX-loaded PCL microparticles within hybrid scaffolds exhibited a controlled release pattern and promoted osteogenic differentiation during the sustained release period through a significant increase in osteonectin and COL1A1

*Correspondence:
Parastoo Noory
noory.parastoo@yahoo.com
Ahmad Reza Farmani
ahmadrezafarmani66@gmail.com
Jafar Ai
jafar_ai@tums.ac.ir; jafar_ay2000@yahoo.com
Naghmeh Bahrami
n-bahrami@sina.tums.ac.ir; naghmehbahrami@gmail.com

Full list of author information is available at the end of the article

expression. Also, increased mineralization was demonstrated by SEM and alizarin red staining. This study proposes that drug-loaded 3D-printed hybrid organic-inorganic nanocomposite scaffolds are promising for advanced bone tissue engineering applications.

Highlights

- Layer-by-layer 3D-printing was effectively applied to prepare a biomimetic combined structure composing hard composite (PCL-nHA) and soft hydrogel (Alg-Gel).
- 3D-printing scaffolds were used to control the delivery of dexamethasone (DEX) to enhance bone repair.
- DEX-loaded scaffolds promoted osteogenic differentiation and mineralization of human endometrial mesenchymal stem cells (hEnMSCs).

Graphical Abstract

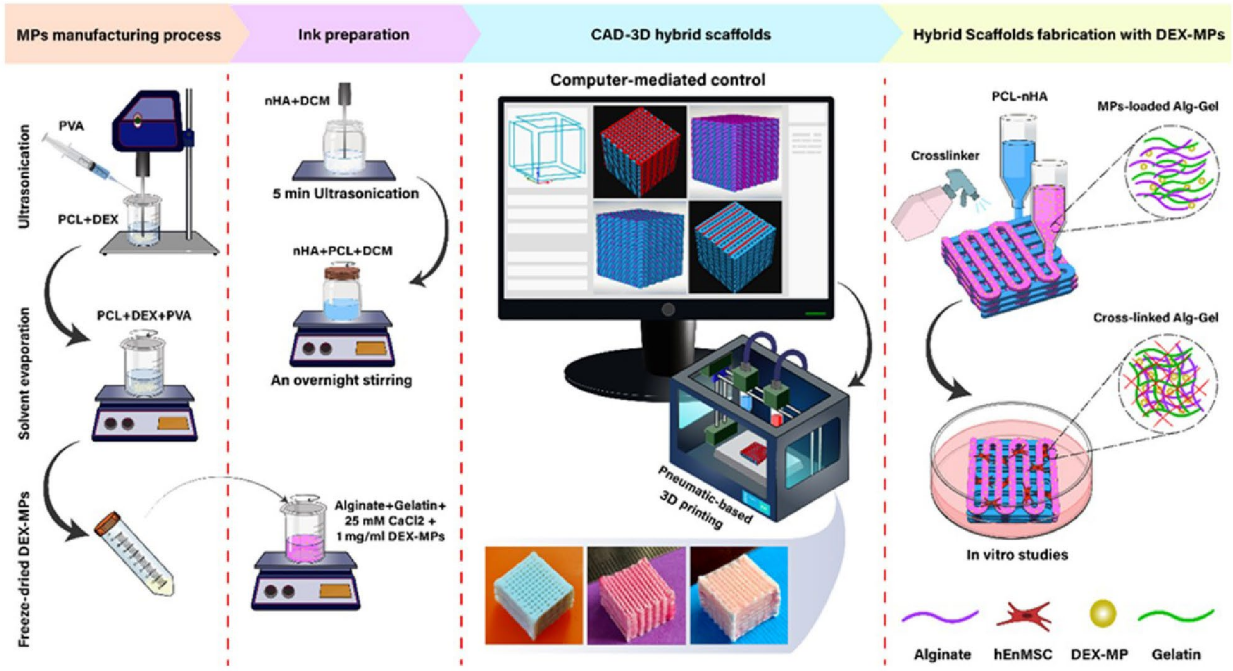

Keywords 3D printing, Layer-by-layer, Polycaprolactone, Nano-Hydroxyapatite, Alginate, Gelatin, Bone tissue engineering, Endometrium-derived mesenchymal stem cells

Introduction

Despite bone tissue has a restricted regenerative capacity, the repair of bone defects exceeding the critical size resulting from tumor resection, infection, or trauma poses a major challenge in the domains of orthopedics and regenerative medicine [1–3]. Consequently, bone is often considered the second most transplanted tissue [4]. The traditional gold standard for the treatment of bone defects has been the utilization of autologous and allograft bone grafts [5, 6]. Nevertheless, the limited availability of bone grafts, the occurrence of additional pain, and the risk of associated diseases have stimulated the development of tissue engineering as an alternative approach [5, 7]. This approach involves three essential components including stem cells, scaffolds, and growth factors, which work together to stimulate the human body towards regenerating bone and repairing bone defects [8]. Stem cells are a promising cell source for bone regeneration due to their ability to self-renew, proliferate, and differentiate [9]. However, stem cells can also be involved in cancer and other pathological conditions [10–14]. Mesenchymal stem cells, particularly endometrial stem cells, have a high ability to proliferate, differentiate, and promote angiogenesis. Endometrial stem cells are easy to harvest and do not cause pain, making them an attractive option for bone regeneration [15, 16].

Growth factors are essential small molecules in tissue engineering, playing a crucial role in cell proliferation, migration, and differentiation [17]. Examples include fibroblast growth factors (FGF), vascular endothelial

growth factors (VEGFs), and platelet-derived growth factor (PDGF), which have demonstrated effectiveness in bone repair [18]. Similarly, osteogenic drugs have been used alone or in combination with growth factors to promote bone regeneration. Hence, both growth factors and drugs are integral components in the development of effective strategies for bone tissue engineering and regeneration [19, 20]. Meanwhile, dexamethasone, a synthetic glucocorticoid, exhibits significant anti-inflammatory properties and exerts a substantial influence on the regulation of genes associated with osteogenesis, or the process of bone formation [21]. Studies have indicated that dexamethasone can stimulate the differentiation of progenitor cells into osteoblasts, thereby facilitating increased bone mineralization [22]. Therefore, the sustained release of dexamethasone from scaffolds represents a promising approach to promote bone regeneration, as demonstrated by several studies [23–25].

Polymers are promising biomaterials in designing controlled drug delivery systems for tissue engineering applications [26–28]. Among synthetic polymers, PCL stands out as highly coveted for drug delivery applications due to its remarkable biocompatibility and degradability as it gradually breaks down within the human body through the hydrolysis of its ester connections [29–31]. Also, previous studies have demonstrated the stable and efficient release of drugs using PCL microparticles (PCL-MPs) [32–34]. However, when it comes to bone tissue engineering (BTE) applications, freely dispersed PCL-MPs may not be suitable. Moreover, hydrogels have great potential in drug delivery and bone regeneration [35]. Hence, incorporating PCL-MPs in hydrogel can be considered as a novel approach for improving controlled drug release and biomimetic bone regeneration [36, 37]. Alginate is a natural polysaccharide known for its excellent biocompatibility and ability to be cross-linked in the presence of polyvalent cations, creating a suitable matrix for encapsulating biological materials [38]. Pure alginate lacks cell-adhesive ligands for mammalian cells, but the addition of gelatin as a denatured form of collagen enables cell adherence and adjusts hydrogel viscosity for extrusion and printing requirements [39]. For instance, Di Giuseppe et al. [40] have demonstrated that the alginate-gelatin composite exhibits favorable viscosity for 3D printing. This composite possesses the capability to encapsulate drug-containing MPs and offers ease of cross-linking, along with suitable degradation characteristics in a porous and cohesive polymer structure, resulting in more stable drug release [41, 42].

Successful bone tissue engineering requires scaffolds with precisely controlled mechanical properties, including sufficient compressive strength and elasticity and easy fabrication processes, in addition to effective drug delivery [43, 44].

Generally, 3D printed scaffolds possess desirable mechanical properties for bone tissue engineering [45]. Research indicates that 3D printed PCL composites especially those reinforced with HA nanoparticles exhibit mechanical properties that closely resemble those of natural bone [46–49]. This similarity is vital to prevent stress shielding and ensure effective load transfer during the healing process. Also, the precision of 3D printing technology allows for the creation of scaffolds with complex architectures that can be optimized for specific mechanical and biological requirements. This customization is essential for developing scaffolds that not only support mechanical loads but also provide a conducive environment for tissue regeneration [50].

These scaffolds must also possess high and interconnected porosity to facilitate vascularization and nutrient transport, promoting stem cell attachment, proliferation, and migration while maintaining adequate mechanical strength to withstand physiological loads [43]. Ideal scaffolds should also be osteoconductive and osteoinductive to enhance osteogenic differentiation [51]. Ceramic biomaterials, such as hydroxyapatite, have widely been used in BTE due to the predominantly mineral nature of bone tissue [52–54]. However, the organic phase of bone extracellular matrix (ECM) has led to the increasing application of biopolymers in bone regeneration [55]. Meanwhile, Polycaprolactone (PCL), a biocompatible and biodegradable thermoplastic polymer, is widely used in additive manufacturing due to its favorable mechanical properties, including high mechanical strength and processability [56–58]. However, PCL alone does not possess osteoinductive properties due to its low cell binding sites and hydrophobicity [59]. To enhance its functionality, researchers have explored combining PCL with calcium phosphate inorganic additives to create functional composites [60]. Nanohydroxyapatite/poly(ε-caprolactone) (nHA/PCL) nanocomposites are fully biodegradable and have widely been investigated for their potential in BTE [61]. These nanocomposites have been shown to promote cell attachment, proliferation, and differentiation, making them a promising option for bone regeneration [62]. Nanocomposites designed for bone regeneration, with their organic and inorganic components, have shown promising results in BTE [63].

Generally, various techniques exist for fabricating scaffolds. Amongst, 3D printing has garnered significant interest among researchers owing to its ability to precisely control the microstructure, porosity, and architecture of scaffolds according to pre-designed patterns using CAD/CAM technology [64]. As a result, 3D printing has been widely employed in the fields of tissue engineering and drug delivery [65–67]. Numerous techniques exist for 3D printing, with the extrusion method being the most commonly used [68]. The extrusion method stands out owing to its advantages comprising high printing speed and the ability to print multiple materials simultaneously

[69]. Despite the numerous benefits of 3D printing, the complexity of the bone structure and its layer-by-layer composition has presented challenges in mimicking its extracellular matrix (ECM) microstructure using 3D-printed scaffolds [70, 71]. Consequently, techniques such as layer-by-layer technology have been widely utilized in the development of bone tissue engineering scaffolds [72, 73]. Therefore, it seems that the combination of these methods, along with the layer-by-layer 3D printing approach, holds promise for the creation of scaffolds with controlled microstructure and biomimetic properties.

Hence, in this study, we used an alginate-gelatin hydrogel to encapsulate DEX-loaded PCL-MPs for a drug delivery system. Layer-by-layer hybrid scaffolds were fabricated using a pre-designed CAD model and 3D printing technique. DEX, serving as a bone differentiation-inducing factor, was loaded into PCL-MPs and printed within the alginate-gelatin hydrogel along with the hybrid scaffolds. The release of the drug from the MPs trapped in the scaffold was evaluated, and its osteogenic induction effects on endometrial mesenchymal stem cells (hEnMSCs) within the scaffold were assessed in vitro.

Materials and methods

Materials

The materials used in this research are listed as follows: Polycaprolactone (PCL, Mw = 80,000, Sigma-Aldrich); Calcium chloride dihydrate ($CaCl_2$, Merck); Alginic acid sodium salt (viscosity: 15–25 cP, 1% in H2O, Sigma-Aldrich USA); Gelatin (Type A, ~300 g Bloom, Sigma-Aldrich USA); Nano Hydroxyapatite (Size range < 20 nm, Apatech, Iran); Dimethyl sulfoxide (DMSO, Sigma Aldrich USA); Glutaraldehyde (Merck KGaA, Darmstadt, Germany); Paraformaldehyde (Sigma-Aldrich USA); Dexamethasone (DEX, HPLC grade, ≥ 98%, Sigma-Aldrich USA); Poly(vinyl alcohol) (PVA, Mw: 72,000, Merck Germany); Dichloromethane (DCM, CH_2Cl_2, Merck Germany); Simulated body fluid (SBF, 1X, Partikan Biomaterial Group, Iran); Alizarin red kit (CM-0058, Lifeline Cell Technology Company, USA); Dulbecco Modified Eagle's Medium (DMEM, Bioidea, Iran); Phosphate-buffered saline (PBS, Bioidea, Iran) tablet; Penicillin/streptomycin (Bioidea, Iran); Collagenase I (Sigma-Aldrich); Fetal bovine serum (FBS, Gibco BRL USA); Trypsin-EDTA 0.25% (1X, Bioidea, Iran); Dimethyl sulfoxide (DMSO, cell culture grade, DNAbiotech, Iran); Amphotericin B (Sigma-Aldrich); Gentamycin (Iran); Flask T-75 (Gibco); Flask T-25 (Gibco); Cell strainer 40, 70, 100 (Gibco); Cell filter 0.2 (Gibco USA); ALP assay Kit (102 395 H917, Pars Azmun Company, Iran); Hydrochloric acid 37% (Merck Germany); hydroxide (NaOH, Merck Germany); cDNA synthesis kit (A101161, Parstous Company, Iran); RNA extraction kit (RiboEx, GA-301-001, GeneAll Biotechnology Company, Korea); DAPI (4′,6-diamidino-2-phenylindole, 1:300,000, Sigma-Aldrich Company, USA).

PCL-DEX microparticles preparation

The fabrication method of PCL-DEX microparticles is according to our previous report [74]. Briefly, it can explain that PCL-DEX microparticles were prepared using a single oil-in-water (O/W) emulsion/solvent-evaporation method. Initially, a mixture of dichloromethane (DCM), and ethanol (1:1, v/v) was used to dissolve 5%, 10%, and 15% (w/w, relative to polymer weight) DEX [75], which was then combined with 5% (w/v) PCL (Mw = 80,000, Sigma-Aldrich) in DCM (1:3, v/v). The resulting mixture was sonicated for one minute at 45% amplitude with 0.5 s on/off using a Q500 sonicator from QSonica in Newton, CT. Then, 10 ml polyvinyl alcohol (PVA, 3% in distilled water), was added to the PCL-DEX solution, and the resulting mixture was sonicated for 3 min at 50% amplitude with 0.5 s on/off. Next, the solution was mixed with 1.5 times the amount of 0.1% PVA and stirred (600 rpm) with a magnetic stirrer for 4 h at room temperature to evaporate the organic solvents. Finally, the solution was centrifuged at 12,000 rpm at 4 °C for 4 min using a refrigerated centrifuge, three times, to eliminate any untrapped drug and PVA residue. The resulting MPs were resuspended in 2 ml of 0.5% sucrose in distilled water (w/v), transferred to a freezer at -80 °C for 24 h, and then subjected to freeze-drying.

PCL-nHA nanocomposite paste preparation

PCL-nHA (50:50, w/w) composite was synthesized by dispersing 1.65 g of nHA into 3 ml of DCM, followed by 5 min ultrasonication (Q500 sonicator, QSonica, Newton, CT) to prevent nHA particle agglomeration. Subsequently, 1.65 g of PCL was added and the resulting slurry was continuously stirred in a sealed container overnight to attain homogeneity of the composite paste [76, 77].

MPs-Incorporating in Alg-Gel hydrogel preparation

In the study, 80 mg/ml alginic acid sodium salt (Sigma-Aldrich USA) was dissolved in 25 mM $CaCl_2$ solution in distilled water containing DEX-loaded MPs (DEX-MPs) suspended at 1 mg/ml, followed by the dissolution of 90 mg/ml gelatin. The resulting prepolymerized hydrogel, which exhibited desirable 3D-printing viscosity, was transferred to a plastic syringe with a 22-gauge blunt dispensing needle [42]. Furthermore, the presence of DEX-MPs in the 3D-printed composite hydrogel was visualized using FESEM (MIRA3TESCAN-XMU, Czech Republic).

Fabrication of hybrid 3D-Printed scaffolds

In this research, two scaffold design strategies were evaluated. The first design strategy involved creating a

layer-by-layer hybrid scaffold consisting of PCL-nHA and Alg-Gel-MPs layers (Hyb-1). The scaffold was built up to 12 layers, with specific dimensions of 12.5 × 12.5 mm, a thickness of 0.5 mm, an inter-filament space of 0.5 mm, and a layer height of 0.2 mm. For the second strategy, a 12-layer scaffold of PCL-nHA composite was designed with the same layer parameters as the first strategy, except that Alg-Gel-MPs were printed every other filament between the PCL-nHA filaments and every two layers (Hyb-2). The hypothesis was that the latter scaffold design would exhibit superior mechanical properties and adequate porosity.

For the experimental setup, a two-nozzle pneumatic 3D printer was utilized, which was set to a perimeter speed of 5 mm/s and a z-axis height of 0.2 mm. The PCL-nHA paste was extruded through a 21-gauge needle using an air pressure of 5–8 bar, while the Alg-Gel-MPs paste was extruded through another needle with 22-gauge and an air pressure of 6–8 bar. After printing each layer of Alg-Gel-MPs, a 30-second pause was applied, and 2 M $CaCl_2$ solution was sprayed onto the hydrogel layer. This crosslinking process through in situ layered spraying of $CaCl_2$ leads to improving structural integrity in Alg-Gel-MPs layers, which is crucial for facilitating the 3D printing of multi-layers, and creating hybrid scaffolds [78–80]. Moreover, other research groups have described the use of bioprinting techniques that employ hydrogels in conjunction with a secondary nozzle. This secondary nozzle is utilized for the deposition of crosslinking agents or the application of a crosslinking solution via a spraying mechanism [80, 81]. Following the procedure, the crosslinking process of the 3D-printed hybrid scaffolds was completed by immersing them in $CaCl_2$ solution for 20 min and 0.5% (v/v) glutaraldehyde solution for one hour. The scaffolds were then rinsed three times with PBS and freeze-dried for 24 h. The configuration of strands and the dimensions of porosities were observed using scanning electron microscopy (SEM, VEGA\\TESCAN-XMU, Czech Republic).

Material characterizations

Encapsulation efficiency

The amount of DEX remaining in the waste PVA solution was used to evaluate the drug encapsulation efficiency of the MPs. The evaluation was carried out using a UV-vis spectrophotometer (Perkin Elmer, USA) at λ-max 242 nm, according to the calibration curve, to optimize the quality and effectiveness of the MPs in drug delivery. The percentage of drug encapsulation efficiency (EE) was calculated using Eq. (1):

$$EE\ (\%) = 1 - \frac{DEX\ amount\ in\ supernatant}{Initial\ \ DEX\ amount} \times\ 100 \quad (1)$$

All measurements were performed in three repetitions and the results are reported as average and standard deviations.

Size, FESEM, and zeta potentials

After freeze-drying, the microparticles were coated with a thin layer of Au-alloy (approximately 10 nm) and subsequently analyzed for morphology and uniformity using field emission scanning electron microscopy (FESEM, MIRA3TESCAN-XMU, Czech Republic). Also, the particle size and zeta potential were determined by dynamic light scattering (DLS, Malvern Nano ZS ZEN3600). To conduct the DLS measurements, one milligram of microparticles was suspended in 50 ml of distilled water and transferred to a plastic cuvette. The sample was then subjected to brief ultrasonication in an ultrasonic bath (JP-010 S, Skymen, China) to prevent particle agglomeration before the analysis. DLS measurements were performed at 25 °C in three replicates to examine mean and standard deviation. Additionally, Fourier transform infrared (FTIR, NEXUS 670 Spectrometer, USA) spectroscopy was used to analyze the chemical structure of PCL-DEX microparticles, as well as PCL and DEX separately, to confirm the presence of DEX within the MPs. To carry out the analysis, the MPs were mixed with KBr, transformed into a disk, and subsequently analyzed over the range of 4000–450 cm^{-1} with a resolution of 1 cm^{-1}.

Drug loading

In order to determine the percentage of MPs in DEX, 3 mg of MPs containing DEX were dissolved in 10 mL of dichloromethane (DCM) to completely degrade the MPs and release the drug. Next, 30 mL of phosphate-buffered saline (PBS) was added and stirred using a magnetic stirrer at 60 °C under a fume hood to completely evaporate the DCM and obtain a solution of PBS and DEX. The solution was then centrifuged at 12,000 rpm for 30 min at 4 °C, and the supernatant was analyzed at a maximum wavelength of 242 nm using a PBS blank. The drug loading efficiency (DLE) percentage was subsequently calculated in Eq. (2):

$$DLE\,(\%) = \frac{\begin{matrix}Mass\ of\ DEX\ determined \\ in\ the\ microparticle\end{matrix}}{\begin{matrix}Mass\ of\ PCL- \\ DEX\ microparticles\end{matrix}} \times 100 \quad (2)$$

It is important to note that all measurements were performed in triplicate, and the reported results are presented as the average and standard deviation.

Drug release study

To assess the drug release pattern from the scaffold, the scaffolds ($n = 3$) were submerged in 5 ml of PBS and

maintained at 37 °C while being agitated at 100 rpm. At specified time intervals, the PBS was sampled, and an equal volume of fresh PBS was used to replace it. The released DEX was quantified at λ-max 242 nm using a UV-Vis spectrophotometer (Perkin Elmer, USA), following the standard calibration curve of DEX.

Upon reaching the final time point, the printed scaffolds were crushed and dissolved in a solution comprising 5 ml of PBS and 5 ml of DCM. This mixture underwent 60 min of ultrasonication (Q500 sonicator, QSonica, Newton, CT), followed by stirring at 60 degrees until DCM completely evaporated, leaving behind a PBS solution containing the drug [74]. This resultant solution was subjected to three rounds of centrifugation at 4 °C for 30 min at 12,000 rpm, and the supernatant was then assessed at λ-max 242 nm using a UV-Vis spectrophotometer (Perkin Elmer, USA).

The total quantity of loaded dexamethasone included the sum of the concentration obtained after crushing and the cumulative concentration of DEX at the final time point. Subsequently, the graph representing the cumulative percentage of drug release was derived using Eq. (3):

$$CDR\,(\%) = \frac{\begin{array}{c}Amount\ of\ DEX\\ released\ at\ time\ \ (t)\end{array}}{\begin{array}{c}Total\ amount\ of\ drug\\ in\ the\ system\end{array}} \times 100 \qquad (3)$$

To elucidate the drug release behavior of DEX from free MPs (MPs-DEX) and the MPs-DEX entrapped in the Hyb-1 scaffold (Hyb-1-MPs-DEX), the release profiles were fitted to various common kinetic models, namely, zero-order, first-order, Korsmeyer-Peppas, Higuchi, Hixson-Crowelland models [82]. The goodness-of-fit for each model was evaluated using the coefficient of determination (R^2). The model equations and parameters are summarized in Table 4.

XRD, and FTIR spectrums

The chemical bonds and functional groups of the initial materials in the nHA-PCL and alginate-gelatin composites were identified using FTIR (FTIR, NEXUS 670 Spectrometer, USA). X-ray diffraction (XRD, D8 ADVANCE, Bruker, Germany), with CuKα radiation at 40 kV and 30 mA, was utilized to identify the crystal phase of the components of the nHA-PCL composite. The scan was performed within a 2θ range of 5–80° at a scanning rate of 1°/min and a count time of 10 s.

Mechanical properties

The mechanical properties of the scaffolds were examined using a universal testing machine (STM-20, SANTAM, Iran). Scaffolds with dimensions of $12 \times 12 \times 12$ mm^3 ($n = 5$) were prepared and subjected to compression testing. A load cell with a capacity of 50 kN and a crosshead speed of 0.5 mm/min was used to perform the test.

Degradation study

The scaffolds ($n = 4$) were incubated in PBS at 37 °C for 12 weeks, after which they were removed periodically every week, gently rinsed with distilled water three times, and oven-dried at 50 °C for 6 h. The dry weight of the scaffolds was measured and the weight loss was eventually calculated using Eq. (4):

$$Weight\ loss\,(\%) = \frac{W_0 - W_t}{W_0} \times\ 100 \qquad (4)$$

Where W_t is the dry weight of the scaffold at time t and W_0 is the initial dry weight of the scaffold before soaking.

Biological assessments

hEnMSCs isolation and characterization

hEnMSCs were isolated following the ethical guidelines of Tehran University of Medical Science, Iran (IR.TUMS.MEDICINE.REC.1399.201). Biopsy samples were obtained from women aged 25 to 30 years, who provided informed consent. The samples were transferred to the laboratory in PBS supplemented with antibiotics. Following washing and chopping, the samples were then incubated in DMEM-F12 supplemented with collagenase I (2 mg/ml) at 37 °C and 5% CO_2 for 30 min, with intermittent shaking. After digestion, the samples were filtered through 70 µm and 40 µm cell strainers and subsequently centrifuged at 1200 rcf for 5 min. The resulting cell pellet was cultured in DMEM-F12 enriched with 10% FBS and 1% penicillin-streptomycin. The medium was changed every three days, and hEnMSCs were passaged using trypsinization at 80% confluency [83]. For all experiments, hEnMSCs at passage three were used. hEnMSCs were then characterized using flow cytometry for MSCs surface markers CD90 and CD105, as well as hematopoietic cells surface markers CD45 and CD34.

Biocompatibility assessments (MTT)

Three groups of scaffolds were studied: PCL-nHA composite scaffold (PCL-nHA), hybrid scaffold built through a layer-by-layer approach, incorporating PCL-nHA and Alg-Gel (Hyb-1), and layer-by-layer hybrid scaffolds incorporating microparticles loaded with dexamethasone (Hyb-1-DEX). To evaluate cell adhesion, the scaffolds in each group were sterilized with 70% ethanol for 30 min and exposed to UV radiation for 1 h on both sides. They were then prewashed in complete medium culture (CMC) supplemented with 10% FBS and 1% penicillin-streptomycin and incubated overnight at 37 °C and 5% CO_2. The next day, the CMC was removed, and the

scaffolds were seeded with 0.3×10^6 hEnMSCs in 100 µL of CMC, allowing for a minimum of 4 h for cell-scaffold interaction. Following this, 1 mL of CMC was added, and the scaffolds were incubated for 5 days. Subsequently, hEnMSCs were fixed on the scaffold using 2.5% glutaraldehyde for 1 h, dehydrated with ethanol (30, 50, 70, 90, and 96% sequentially) for 5 min each, and air-dried overnight at room temperature. The SEM (VEGA\\TESCAN-XMU, Czech Republic) technique was employed to observe the morphology of hEnMSCs on the scaffolds.

The MTT assay was conducted to evaluate scaffold cytotoxicity. Initially, hEnMSCs were seeded onto the scaffold (at a density of 10×10^3 cells per well in a 96-well plate) and incubated at 37 °C with 5% CO_2 for 1, 3, and 5 days. Subsequently, the culture medium was replaced with 100 µl of RPMI containing 10% (v/v) MTT, followed by a 4-hour incubation period. Afterward, the RPMI solution was aspirated from each well and transferred to a separate 96-well plate, and 100 µl of DMSO was added. The plate was agitated for 5 min, and the absorbance at a wavelength of 570 nm was measured using an ELIZA reader (ELX808, Bio-Tek, USA).

Alizarin red staining

Alizarin Red staining (ARs) was performed to evaluate calcium deposition as an indicator of successful differentiation of hEnMSCs into osteoblasts using both direct and indirect procedures.

In the direct method, scaffolds were seeded with 10×10^4 MSCs in a 24-well plate, and the medium was changed every 3 days until days 14 and 21. At each time point, the medium was discarded, and the scaffolds were rinsed with PBS, fixed with 4% paraformaldehyde (Sigma-Aldrich USA) at room temperature for 1 h, and subsequently stained with ARs (2% in distilled water, pH = 4.1–4.3) for 45 min. The scaffolds were then photographed and observed using an inverted microscope after being rinsed with distilled water (3 times). To quantify staining, 10% acetic acid was added to the wells and incubated at room temperature for 30 min to extract ARs bound to calcium deposits and subsequently neutralized using 10% ammonium hydroxide. The plate was examined at a wavelength of 405 nm, and the optical density (OD) obtained was subtracted from the OD obtained from the control group (unseeded scaffold). The results were quantified using a calibration curve based on known concentrations of ARs. The tests were performed in triplicate.

Moreover, in the indirect method [84, 85], scaffolds in different groups were incubated with medium in a 24-well plate at 37 °C with 5% CO_2 for 7, 14, and 21 days. On the other hand, MSCs were cultured (60×10^3 cells per well) in another 24-well plate and treated with scaffold extraction when they reached 90% confluency. The medium was substituted with scaffold extraction every three days, and a fresh medium was added to the scaffold wells. At each time point, MSCs were gently washed with PBS and fixed with 4% paraformaldehyde (Sigma-Aldrich USA) at room temperature for 1 h. Subsequently, they were stained with Alizarin Red (2% in distilled water, pH = 4.1–4.3) for 45 min after rinsing with distilled water twice. Alizarin Red was then removed, and the cells were washed twice with distilled water. 1 ml of PBS was added to each well for visualization and photography using an inverted confocal microscope.

In vitro bioactivity analysis

The formation of apatite nuclei was determined using simulated body fluid (SBF). The required amount of SBF for each scaffold was calculated by Eq. (5) [86]:

$$V_s = S_a/10 \tag{5}$$

where S_a represents the apparent surface area of the scaffold (mm^2), and V_s represents the required amount of SBF (ml).

The scaffolds were incubated with SBF in sealed plastic bottles and kept at 37 °C for 7, 14, 21, and 28 days. At each time point, the samples were taken out, rinsed gently with distilled water, and then dried in a desiccator. Apatite crystal precipitation was subsequently observed using FESEM (MIRA3TESCAN-XMU, Czech Republic), and the chemical composition was analyzed by Energy Dispersive Spectroscopy (EDS).

Gene expressions

The gene expression levels of collagen I (COL1A1), osteonectin (OST), and RUNX2 were evaluated during osteogenesis differentiation at 14 and 21 days. RNA was extracted from MSCs cultured on 3D-printed scaffolds using a GeneAll® RiboEx RNA extraction solution (GeneAll Biotechnology, Korea) and then reverse transcribed into cDNA using a reverse transcription kit (Parstous Company, Iran). Real-time PCR reactions were performed using specific primers targeting COL1A1, OST, and RUNX2 genes. The PCR program involved cycling stages of denaturation, annealing, and extension. The expression levels of the genes were determined using the comparative threshold cycle (Ct) method. The obtained data were subsequently analyzed to assess the osteogenic differentiation of hEnMSCs based on the expression levels of these genes. Primers were used for gene expression study are presented in Table 1.

Alkaline phosphatase assay (ALP)

Alkaline phosphatase, an enzyme highly expressed in the early stages of osteogenic differentiation, serves as an indicator for differentiating MSCs into osteoblasts.

Table 1 Primer sequences for genes in RT-qPCR

Gene name	Sequence	Annealing temp	Product size (bp)
Osteonectin (OST)	For: 5′- ACATCGGGCCTTGCAAATAC – 3′	60	122
	Rev: 5′- GTTGTCCTCATCCCTCTCAT – 3′		
Collagen I (COL1A1)	For: 5′- GTGCTAAAGGTGCCAATGGT – 3′	60	128
	Rev: 5′- ACCAGGTTCACCGCTGTTAC – 3′		
RUNX2	For: 5′- TAGGCGCATTTCAGGTGCTT – 3′	60	105
	Rev: 5′- TGCATTCGTGGGTTGGAGAA – 3′		
GAPDH	For: 5′- CTCATTTCCTGGTATGACAACG – 3′	60	122
	Rev: 5′- CTTCCTCTTGTGCTCTTGCT – 3′		

OST, Homo sapiens secreted protein acidic and cysteine rich (SPARC); COL1A1, Homo sapiens collagen type I alpha 1 chain; RUNX2, Homo sapiens RUNX family transcription factor 2; GAPDH, Homo sapiens glyceraldehyde-3-phosphate dehydrogenase

ALP enzyme activity was measured according to the standard method of the German Biochemical Society (DGKC) using the kit from Pars Azmoun (Iran). In this method, the sample ALP enzyme hydrolyzes the colorless substrate 4-nitrophenyl phosphate-4 (NPP) at pH 10.3 and a temperature of 37 °C, converting it into yellow 4-nitrophenol.

First, the culture medium was collected from the samples. The cells were washed with PBS and lysed with a specific volume of lysing solution. The protein concentration in a specific volume of each sample was measured using Bradford solution. The same amount of protein was used to measure the enzyme activity. After preparing the working solution according to the kit instructions, 100 µl of the working solution were added to a specific volume of the sample. The changes in color intensity were read over several minutes with a spectrophotometer at 405 nm (ELISA reader Bio Tek ELx808). The final result of the enzyme activity level is reported based on the extracted protein.

Immunocytochemistry analysis

Immunocytochemistry (ICC) staining was performed on hEnMSC-seeded scaffolds. The scaffolds were fixed with 4% paraformaldehyde for 15 min at room temperature to preserve the cellular structure. Permeabilization was done using 0.2% saponin in a blocking buffer (10% goat serum, 10 mM Hepes, 10 mM glycine in RPMI 1640) for 15 min at room temperature, followed by washing and blocking for 1 h at room temperature. Specific antibodies against OST were then incubated with the cells overnight at 4 °C after dilution in the blocking buffer. After three PBS washes, the cells were exposed to secondary antibodies conjugated with Alexa488 (Invitrogen, 1:100 dilution). Slides were mounted with Prolong Gold anti-fade reagent containing DAPI for preservation and photographed using inverted fluorescence microscopy (Leica, TCS SP-8, Germany).

Table 2 EE, DL and PS of PCL-microparticles. In the drug/polymer ratio of 3:20, the highest entrapment efficiency and drug loading have been achieved

Drug/polymer ratio (w/w)	EE (%) ± SD	DL (%) ± SD	PS (µm) ± SD
1:20	55.36 ± 2.614	4.54 ± 0.385	0.784 ± 0.126
1:10	78.28 ± 1.348	8.76 ± 0.251	0.837 ± 0.131
3:20	85.09 ± 1.775	14.34 ± 0.157	1.138 ± 0.147

Note: Data is presented as mean ± SD

Statistical analysis

Statistical analysis of the groups was performed using SPSS version 2023 software. ANOVA software was employed to compare between groups, supplemented with Tukey's test. The results were reported in terms of mean and standard deviation. Statistical significance levels of $^{*}p \le 0.05$, $^{**}p \le 0.01$, and $^{***}p \le 0.001$ were considered.

Results

Characterization of DEX-MPs

DEX-MPs were synthesized through a water-in-oil solvent evaporation/extraction technique. To ensure the optimal manufacturing process for achieving desirable morphology, particle size (PS), and higher values of encapsulation efficiency (EE) and drug loading (DL) of the DEX-MPs, we conducted various experimental tests. Initially, we adjusted various drug-to-polymer ratios (1:20, 1:10, 3:20) to optimize encapsulation efficiency percentage, drug loading percentage, and particle size. The summarized results are presented in Table 2. Among these ratios, the 3:20 ratio exhibited significantly higher percentages of EE and DL compared to other drug-to-polymer ratios. Consequently, the 3:20 ratio was selected for subsequent tests.

Also, the zeta potential results show that DEX-free MPs have a value of -27.7 ± 0.99, whereas DEX-MPs exhibit a significantly lower value of -31.65 ± 0.07 ($p < 0.01$) (Fig. 1c). This decrease in zeta potential indicates an increase in the negative surface charge upon drug loading. More negative zeta potential is advantageous as it enhances the stability of DEX-MPs by promoting repulsion between particles, preventing aggregation, and maintaining their dispersed state. This stability is crucial for achieving controlled drug release and targeted delivery to hEnMSCs. The morphology of MPs was evaluated using FESEM after freeze-drying. The MPs displayed a spherical shape, uniformity, and a smooth surface post freeze-drying (Fig. 1a). Particle size distribution (PSD) analysis conducted through DLS (Fig. 1b) revealed a range of particle sizes from 0.24 to 5.58 µm, with a dominant mode observed at 1.17 µm, aligning perfectly with the FESEM findings.

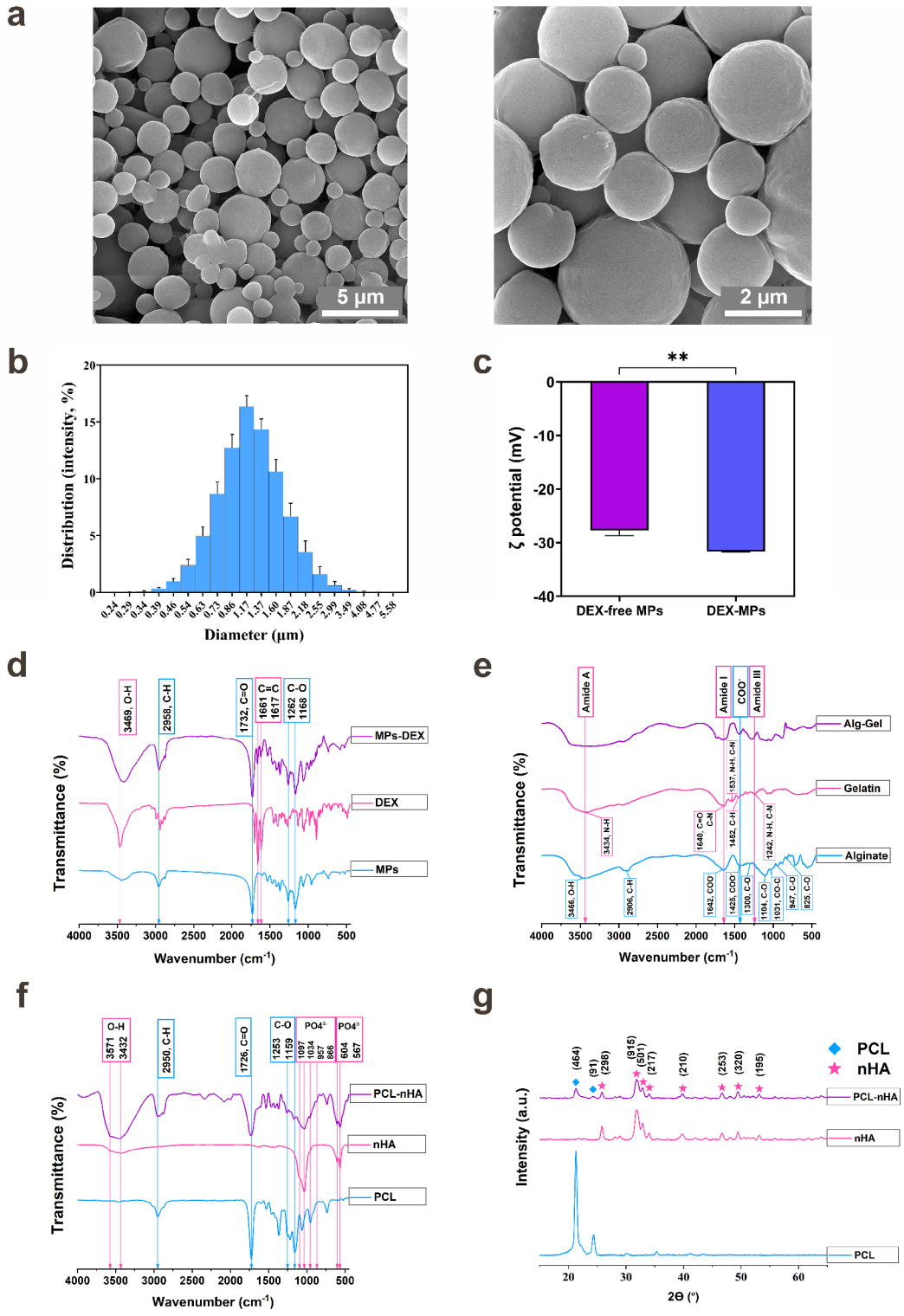

Fig. 1 DEX-MPs characterization and chemical characterization of scaffolds and their ingredients (**a**) FESEM microscope images illustrate PCL MPs loaded with DEX. (**b**) The size distribution diagram of PCL MPs containing DEX was determined by DLS. (**c**) Zeta potential comparison between MPs with DEX and those without DEX. Spherical-shaped uniformly smooth DEX-loaded microparticles with normal size distribution and high stability were produced through the water-in-oil solvent evaporation/extraction technique. (**d**) FTIR spectrum of PCL microparticles loaded with dexamethasone. (**e**) FTIR spectrum of alginate-gelatin composite. (**f**) FTIR spectrum of PCL-nHA composite. (**g**) XRD pattern of PCL-nHA composite. Incorporation of DEX and nHA in PCL have been proved through FTIR and XRD spectrums. ** Indicates a significant difference at the $P < 0.01$ level

FTIR spectroscopy and XRD assessment

The FTIR spectra of MPs, DEX, DEX-MPs, gelatin, alginate, Alg-Gel, PCL, nHA, and PCL-nHA are presented in Fig. 1**(d-f)**. The incorporation of DEX into MPs was verified through FTIR analysis, as shown in Fig. 1d. The FTIR spectrum of pure DEX exhibited absorption peaks at 1617 cm^{-1} and 1661 cm^{-1}, corresponding to C = C stretching vibrations in the drug's structure, while the peaks at 3469 cm^{-1} were indicative of O-H vibrations in DEX. The intensified ester carbonyl peak (C = O) at 1732.43 cm^{-1} confirmed changes in the carbonyl bond due to drug inclusion. In the pure PCL spectrum, the peaks at 1168 cm^{-1} and 1262 cm^{-1} were associated with the C-O stretching vibration bond, and the 1732 cm^{-1} peaks represented the C = O stretching vibration bond, with the 2958 cm^{-1} peak relating to the asymmetric stretching of C-H bond. In the PCL-DEX spectrum, new peaks emerged at 1621.35 cm^{-1}, 1665.15 cm^{-1}, and 3415.03 cm^{-1}, which can be attributed to the presence of DEX [75, 87].

The FTIR spectra of alginate, gelatin, and Alg-Gel composite (Fig. 1e) exhibit broad bands in the 3500–3400 cm^{-1} range, indicating stretching vibrations of N-H and O-H groups, which are also observed in the spectra of pure alginate and gelatin. In the spectrum of alginate, absorption peaks at 1642 and 1425 cm^{-1} represent asymmetric and symmetric stretching vibrations of COO- groups, respectively. Additionally, vibrations at 1300 cm^{-1} correspond to C-O stretching, while vibrations at 1104 and 1031 cm^{-1} signify C-O and CO-C vibrations in mannuronic and guluronic units, respectively. In the gelatin spectrum, stretching vibrations of C-N and C = O groups in amide I are evident at 1640 cm^{-1}, while C-N and N-H vibrations of amide II are observed at 1537 cm^{-1}, and C-N and N-H vibrations of amide III are present at 1242 cm^{-1} [88, 89].

Additionally, analyzing the spectra of the Alg-Gel composite, the asymmetric stretching vibration of COO- in alginate has merged with the stretching vibrations of Amid I and shifted to the absorption band at 1666 cm^{-1}. Peaks at 1434 cm^{-1} represent symmetric stretching vibrations of COO- groups. Peaks at 1087 and 1032 cm^{-1} are associated with C-O and CO-C stretching vibrations, while the peak at 2950 cm^{-1} indicates stretching vibrations of C-H bonds within the alginate component. Additional peaks at 1282, 1731, and 2191 cm^{-1} suggest potential chemical interactions between the two substances. These findings confirm the successful combination of alginate and gelatin in the composite material [88, 90].

The FTIR spectrum of the PCL-nHA biocomposite sample (Fig. 1f) reveals the presence of PCL, as indicated by the distinctive C-O (1159 and 1253 cm^{-1}), C = O (1726 cm^{-1}), and CH2 (2867, 2950 cm^{-1}) peaks. Additionally, the existence of nHA is evident from the characteristic peaks corresponding to PO_3^{-4} (567, 604, 866, 957, 1034 and 1097 cm^{-1}) and O-H (3432 and 3571 cm^{-1}) groups [91, 92]. Additionally, the emergence of supplementary peaks in the hybrid spectrum, at 1997, 2080, 2337, 2708, and 3914 cm^{-1}, suggests the existence of interactions between PCL and nHA. This may indicate potential chemical bond formation or structural rearrangements. These results validate the presence of both materials within the composite [91–93].

The XRD analysis was performed on nHA, PCL, and the PCL/nHA composite film, as illustrated in Fig. 1g. Alongside the characteristic diffraction peaks of nHA, the PCL/nHA composite film exhibits two distinct peaks at 2θ values of 21.18 and 24.2 degrees. These peaks correspond to the (464) and (91) crystallographic planes of pure PCL, respectively. These findings highlight the presence of a semi-crystalline phase within the PCL/nHA composite film. Importantly, the absence of new peaks or shifts in existing peaks within the PCL/nHA composite film suggests that the structural integrity of both PCL and nHA components remains unchanged [94].

Morphological findings (Optical Images)

In this study, scaffolds of PCL-nHA, Hyb-1 (Alg-Gel and PCL-nHA composites are printed layer by layer simultaneously), and Hyb-2 (Alg-Gel hydrogel is printed every other filament between the PCL-nHA filaments and every two layers) were designed using CAD software. Optical images of the 3D printed constructs revealed distinct materials in the upper and lateral views (Fig. 2). The PCL scaffold, printed using DCM solvent, exhibited high viscosity, resulting in a disordered structure and a high decrease in dimensions with increasing layers. Hence, due to its highly irregular dimensions, its compressive strength was not be able to be measured. It seems that incorporating additives and alternative printing techniques may enhance the quality of this particular polymer. Interestingly, incorporating the biocompatible nHA component into PCL led to a significant improvement in printability. Therefore, an optimal composition was used in this study for 3D printing led to the development of PCL-nHA composite scaffolds with uniform pore and fiber sizes and dimensions, displaying high reproducibility.

However, regarding the scaffold based on Alg-Gel hydrogel, an increase in the number of printed layers resulted in progressively smaller pore sizes and layer collapse. Similarly, due to the considerable deterioration of 3D printed structures and changes in dimensions, the compressive strength of this scaffold could not be measured. Although printing both the Hyb-1 and Hyb-2 scaffolds exhibited integrated structures with regular

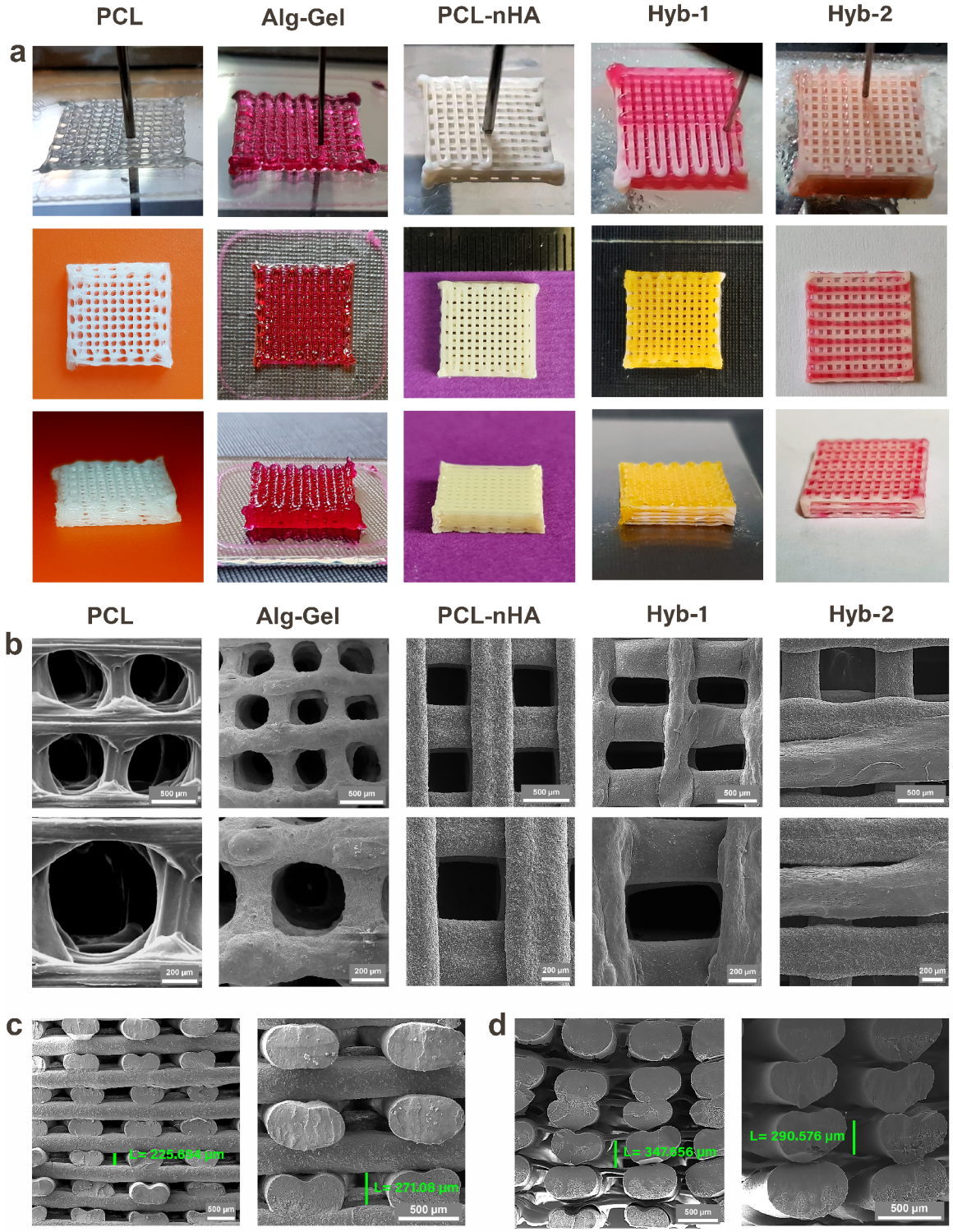

Fig. 2 Top and lateral views and SEM images of the 3D scaffolds; (**a**) Top and lateral views of PCL, Alg-Gel, PCL-nHA, Hyb-1 and Hyb-2 3D printed scaffolds. The structure of Hyb-1 exhibited greater regularity and higher porosity compared to Hyb-2 and PCL-nHA. (**b**) SEM images of Top views of PCL, Alg-Gel, PCL-nHA, Hyb-1, and Hyb-2 3D printed scaffolds. (**c**) SEM images of Cross-sectional views of PCL-nHA and (**d**) SEM images of Hyb-1 scaffolds (scale bars = 200 µm, 500 µm). Hyb-1 microstructure is regular and has a larger pore size than PCL-nHA and Hyb-2 scaffolds

Table 3 Evaluation of porosity size in scaffolds using ImageJ software and shrinkage assessment

Group	Alg-Gel	PCL-nHA	Hyb-1	Hyb-2
Shrinkage (%)	35.99 ± 2.09	5.37 ± 0.677	14.07 ± 2.53	9.93 ± 1.95
Pore Size (μm)	392.52 ± 11.42	474.2 ± 9.2	368 ± 17 × 681 ± 28	451 ± 21

Note: Data is presented as mean ± SD

layering, maintaining the desired and uniform size of fibers and pores.

Microscopic studies (SEM Images)

Observing the SEM images (Fig. 2a-c), it is evident that the scaffolds exhibit straight filaments and uniform pore sizes in scaffolds. Specifically, the Hyb-2 scaffold demonstrates well-placed Alg-Gel filament between PCL-nHA strands. After the freeze-drying process, some level of shrinkage occurred in the scaffolds, with the highest amount of shrinkage observed in the Alg-Gel scaffolds. Additionally, Hyb-1 scaffolds displayed dimensional changes in pore size alongside shrinkage. Nevertheless, the overall dimensions of the scaffold approximately remained unchanged, regarding improvement of dimensional stability of Alg-Gel related to the cross-linking and the presence of the PCL-nHA component, which ensured the maintenance of the main framework. Furthermore, when the scaffolds were immersed in an aqueous environment, the hydrogel component re-swelled, causing the pore dimensions to return to their original state. Further details regarding pore sizes and shrinkage are provided in Table 3.

Degradation rate of scaffolds

The degradation behavior of various scaffold types, including PCL, Alg-Gel, PCL-nHA, Hyb-1, and Hyb-2, was assessed in PBS at 37 °C over 12 weeks. The degradation rates of the scaffolds were 3.28 ± 1.04%, 5.74 ± 0.57%, 14.93 ± 3.95%, 39.11 ± 6.08%, and 88.04 ± 6.17% for PCL, PCL-nHA, Hyb-2, Hyb-1, and Alg-Gel, respectively. The degradation diagram (Fig. 3a) illustrates that both PCL and PCL-nHA scaffolds exhibited a slow and consistent degradation pattern throughout all stages. The Alg-Gel scaffolds showed the highest degradation rate, with an initial intensified degradation observed within the first two weeks, followed by a more uniform upward trend over time. Hyb-1 scaffolds demonstrated a higher degradation rate than Hyb-2 scaffolds, attributed to the increased presence of hydrogel within the hybrid scaffolds. However, both Hyb-1 and Hyb-2 scaffolds demonstrated significantly lower degradation rates compared to

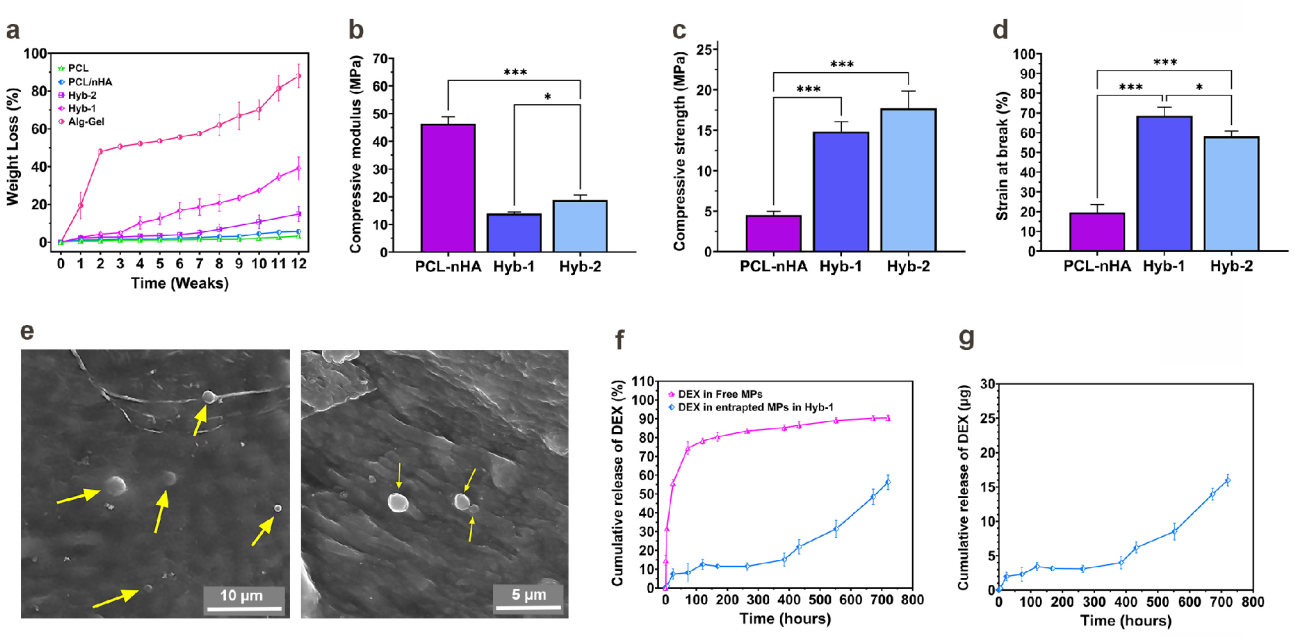

Fig. 3 Degradation Rate, Compressive properties, Morphology and in vitro DEX release from free MPs and entrapped MPs in Hyb-1 scaffolds (**a**) Degradation graph of scaffolds for 12 weeks in PBS. The degradation rate of Hyb-1 is half of Alg-Gel. (**b**) compressive modulus (**c**) compressive strength, and (**d**) strain at failure obtained through compressive testing of scaffolds. Hyb-1 has the most strain at failure and slightly lower compressive strength and compressive modulus than Hyb-2. (**e**) FESEM images illustrating the distribution of MPs within the alginate-gelatin hydrogel. (**f**) Cumulative percentage of DEX released from both free MPs and MPs entrapped in an Alg-Gel. (**g**) Cumulative concentration of DEX released from MPs entrapped in the Alg-Gel. DEX-MPs are uniformly dispersed in the Hyb-1 scaffold and revealed sustained released behavior compared with burst release of DEX from free DEX-MPs. The data is presented as mean ± SD ($n = 3$). *** Indicates a significant difference at the level of $P < 0.001$. * Indicates a significant difference at the $P < 0.05$ level

pure Alg-Gel scaffolds, a trend that aligns logically with their composition.

Mechanical behavior of scaffolds

The scaffold's mechanical properties were evaluated using a compression test. The results, including compressive modulus, strength, and strain, are presented in Fig. 3b-d. The analysis showed that PCL-nHA has a significantly higher compressive modulus than Hyb-1 and Hyb-2 (46.37 ± 2.58 MPa, 13.94 ± 0.62 MPa, and 18.83 ± 1.72 MPa, respectively) and a notably lower compressive strength (4.51 ± 0.47 MPa, 14.84 ± 1.21 MPa, and 17.71 ± 2.14 MPa, respectively). Additionally, Hyb-2 scaffolds exhibited slightly higher compressive strength and modulus compared to Hyb-1 scaffolds. In contrast, Hyb-1 scaffolds showed more strain at break than Hyb-2 scaffolds. Furthermore, both Hyb-1 and Hyb-2 demonstrated significantly higher failure strain than PCL-nHA (68.50 ± 4.33%, 58.15 ± 2.72%, and 19.66 ± 4.04%, respectively).

The observed trend can be ascribed to the decreased porosity and denser structure of the Hyb-2 scaffolds, resulting in enhanced mechanical properties. Analysis of the data indicated that PCL-nHA scaffolds exhibited a more brittle behavior compared to the other two types. Conversely, Hyb-1 scaffolds demonstrated a more flexible behavior, possibly due to the higher content and flexibility of the polymer component within the scaffolds.

Table 4 The results of fitting different kinetic models for the release of DEX from MPs-DEX and Hyb-1-MPs-DEX

Fitting models			Systems	
Models	**Equations**	**Parameters**	**MPs-DEX**	**Hyb-1-MPs-DEX**
Korsmeyer-Peppas	$F = k_{KP}t^n$	R^2	0.949	0.918
		K_{KP} (h^{-n})	29.313	0.002
		n	0.181	1.629
Higuchi	$F = k_H t^{0.5}$	R^2	0.455	0.740
		K_H ($\mu g.ml^{-1}.h^{-1/2}$)	4.268	1.388
Hixson-Crowell	$F = 100(1-(1-k_{HC}t)^3)$	R^2	0.494	0.857
		K_{HC} ($\mu g^{1/3}.ml^{-1/3}.h^{-1}$)	0.002	0.000
First-order	$F = Fmax(1-e^{-k1t})$	R^2	0.948	0.882
		K_1 (h^{-1})	0.058	0.000
Zero-Order	$F = F0 + k_0 t$	R^2	0.526	0.885
		K_0 ($\mu g.ml^{-1}.h^{-1}$)	0.085	0.064

Model parameters. F: the fraction of DEX released at time t. F0: the initial fraction of DEX during burst release. Fmax: the maximum fraction of DEX released at infinite time. k0: the zero-order release constant. k1: the first-order release constant. k_H: the Higuchi release constant. k_{HC}: the Hixson-Crowell release constant. k_{KP}: The release constant that takes into account the geometrical and structural properties of the drug dosage form. n: the diffusional exponent indicating the mechanism of DEX release. $n \leq 0.45$: Fickian diffusion; $0.45 < n < 0.89$: anomalous and non-Fickian diffusion; $0.89 < n < 1$: zero-order and non-Fickian Case-II transport (polymer relaxation); $n > 0.89$: super Case-II transport [95, 96]

In vitro DEX release from free MPs and entrapped MPs in Hyb-1 scaffolds

The analysis of the field-emission scanning electron microscopy (FESEM) images of Hyb-1-DEX clearly demonstrates the successful encapsulation of DEX-MPs within the hydrogel matrix, as indicated by the yellow arrows (Fig. 3e). The microparticles were uniformly distributed throughout the hydrogel structure, retaining their initial uniformity without deformation after being incorporated into the hydrogel. The release profiles of the free MPs-DEX and MPs-DEX entrapped in the Hyb-1 scaffolds were studied over 30 days (Fig. 3f-g). The release of DEX from the free MPs showed an initial burst release of 55.76 ± 1.78% within the first day, gradually increasing to 90.39 ± 1.45% by day 30. In contrast, the MPs-DEX entrapped in the Hyb-1 scaffold exhibited a significantly lower initial burst release of 6.99 ± 2.09% within the first day, followed by a slower and sustained release profile, reaching 55.8 ± 2.89% by day 30. These findings suggest that the presence of the scaffold effectively modulated the release of DEX from the microcarrier system, resulting in a controlled release pattern.

The drug release data from free MPs showed a high correlation (R^2 = 0.949) with the Korsmeyer-Peppas model, as shown in Table 4, indicating that this model is the most appropriate to describe the release kinetics. The Korsmeyer-Peppas exponent (n) was determined to be 0.181. According to the model, when n is below 0.45, it indicates that a Fickian diffusion mechanism primarily governs drug release. This means that the release of DEX from the MPs is driven by the concentration gradient of the drug within the matrix [95]. The first-order model also showed a high correlation (R^2=0.948) with a rate constant (K_1) of 0.058. This model, in conjunction with the Korsmeyer-Peppas model, suggests that the release rate is also dependent on the amount of drug present in the system, which shows a fast release kinetics with an exponential pattern that confirms the dominance of diffusion [82]. The Higuchi, Hixson-Crowell, and zero-order models exhibited poor fits to the data (Table 4), implying that these mechanisms, including matrix erosion and zero-order release, play a minimal role in the drug release from free MPs.

In contrast, the drug release data from the Hyb-1 scaffolds were better described by the Korsmeyer-Peppas model (R^2 = 0.918). However, n was determined to be 1.629. Based on the Korsmeyer-Peppas model, $n > 1$ suggests a non-Fickian transport mechanism, specifically a Super Case-II transport [96]. This indicates that erosion and polymer relaxation control drug release from the Hyb-1 scaffolds in addition to drug diffusion [97]. The zero-order model also displayed a reasonable fit (R^2 = 0.885), indicating a tendency for constant drug release independent of drug concentration [95] after an initial

phase with a rate constant (K_0) of 0.064. The remaining models had comparatively lower fits, confirming the complex release mechanism.

In vitro bioactivity test in SBF

The study used FESEM images to evaluate the formation of hydroxyapatite on scaffolds immersed in SBF for 7, 14, 21, and 28 days. The EDS charts of PCL, PCL-nHA, and Hyb-1-DEX scaffolds on day 28 were also presented (Fig. 4). The analysis of the SEM images revealed that the amount of mineral material formation on the surface of Hyb-1-DEX scaffolds was significantly higher than that of PCL-nHA and PCL at all time intervals. The amount of mineral material formation increased significantly with the immersion time (Fig. 4a). The analysis of the EDS results showed that the ratio of calcium to phosphorus on the surface of the scaffolds was 1.85, 1.6, and 0.64 for Hyb-1, PCL-nHA, and PCL, respectively, indicating that

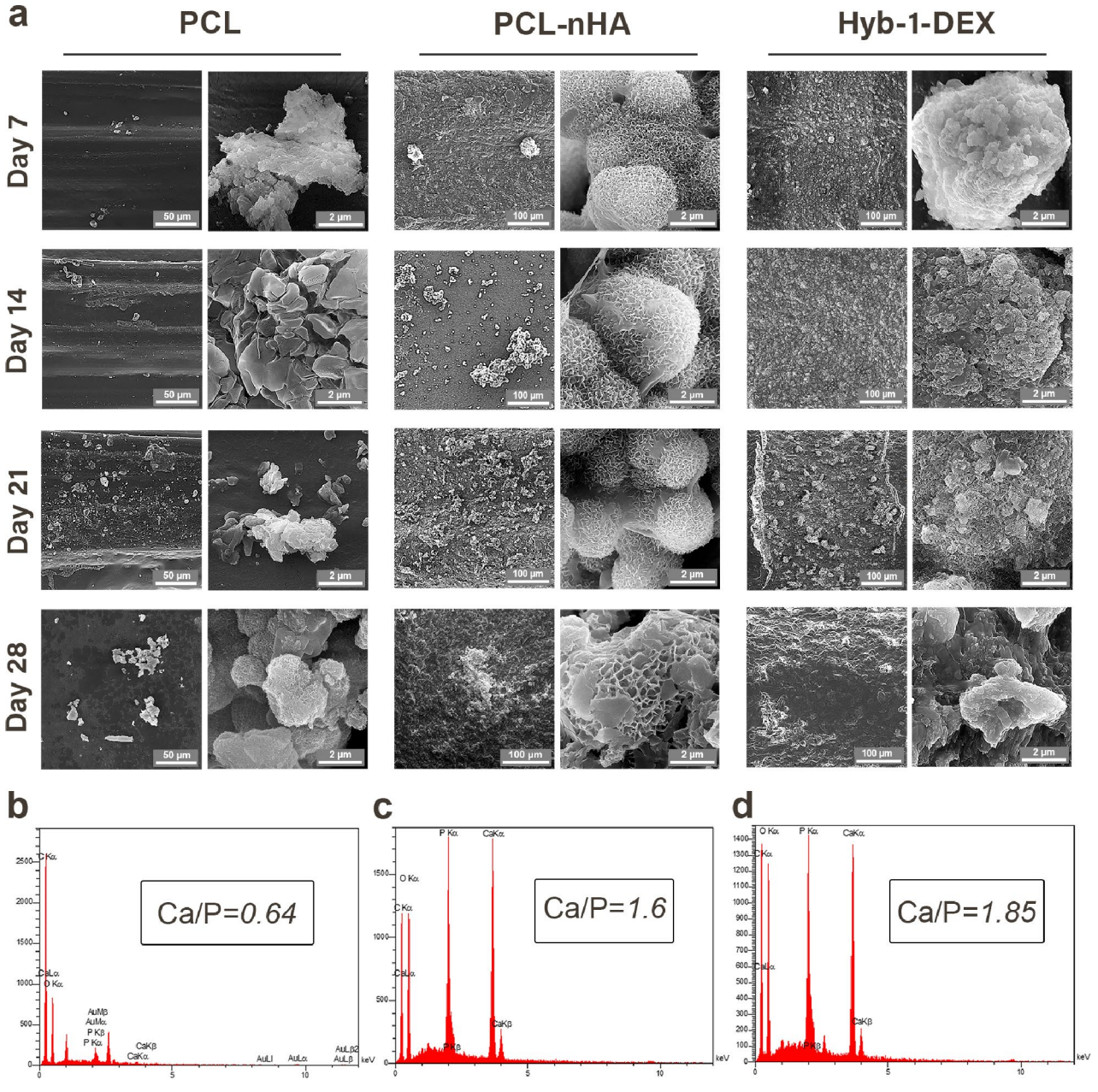

Fig. 4 Bioactivity assessment for PCL, PCL-nHA, and Hyb-1-DEX scaffolds. (**a**) FESEM Imaging of apatite crystals formed on the scaffolds on days 7, 14, 21, and 28 after immersion in SBF. EDS chart of (**b**) PCL (**c**) PCL-nHA and (**d**) Hyb-1-DEX scaffolds on day 28. Higher mineralization can be observed in Hyb-1-DEX scaffolds

the increase in calcium absorption and mineralization may be attributed to biomineralization associated with the presence of DEX in Hyb-1-DEX (Fig. 4b-d).

hEnMSCs isolation and biocompatibility assessment

hEnMSCs were isolated from endometrial tissue and cultured in cell culture flasks. The cells exhibited rapid growth in the culture medium and maintained a consistent proliferative capacity. Within one week of culture, the cells adopted a spindle-shaped fibroblast-like morphology and formed a homogenous monolayer of specific mesenchymal colonies (Fig. 5a). For subsequent tests, hEnMSCs from the third passage were evaluated. To identify the surface markers expressed by hEnMSCs, flow cytometry analysis was performed (Fig. 5b). hEnMSCs exhibited a high expression level of typical MSC-like surface markers, including CD90 (97.7%) and CD105 (99%), while showing a low expression level of blood cell surface markers such as CD34 (1.24%) and CD45 (52%).

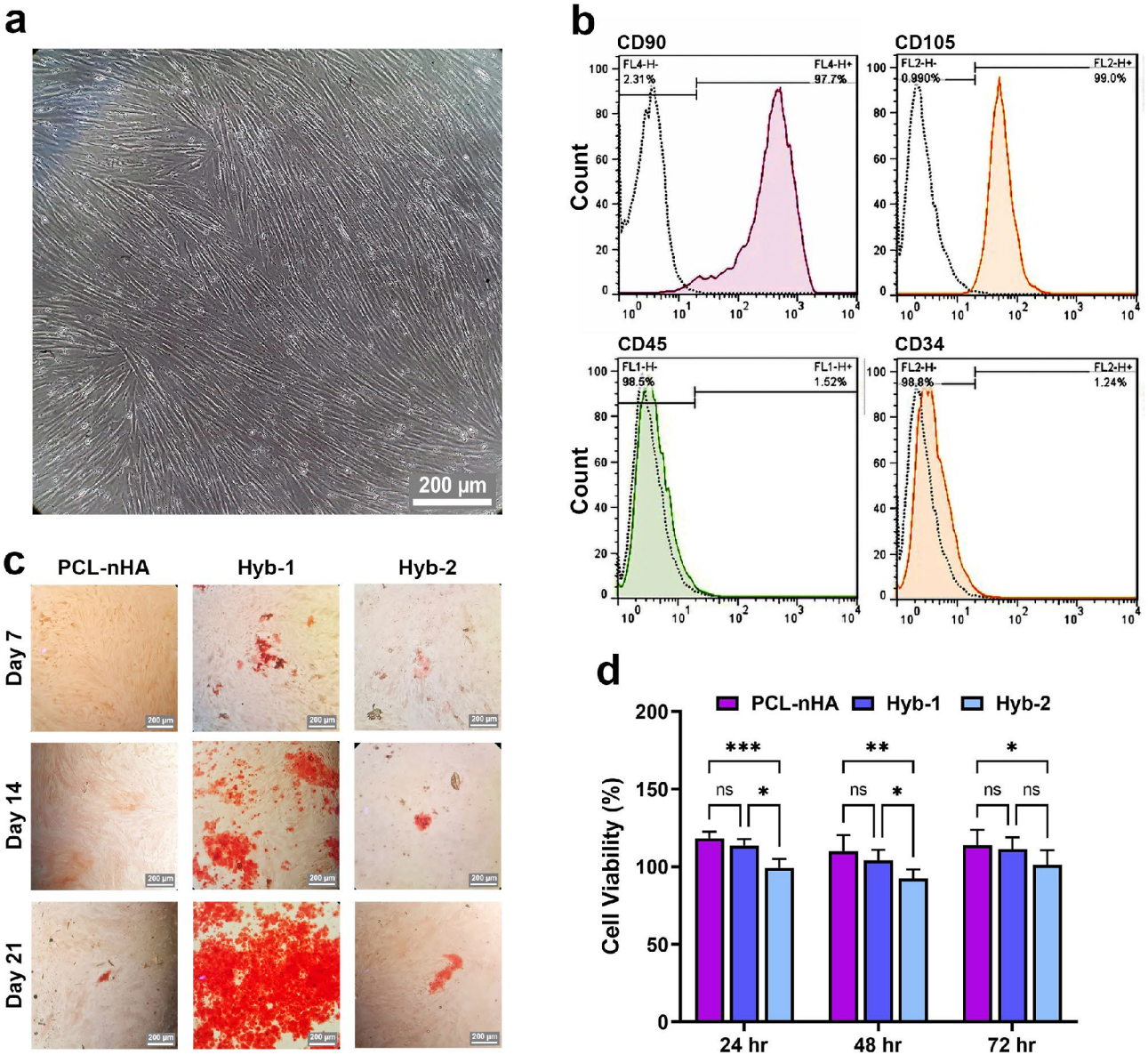

Fig. 5 Identification of hEnMSCs and biocompatibility evaluation of PCL-nHA, Hyb-1 and Hyb-2 scaffolds. (**a**) Colony-forming spindle cells attached to the bottom of the flask with a polyhedral appearance one week after culture (Inverted microscope, magnification: 100X). (**b**) Flow cytometry analysis of hEnMSCs. (**c**) Alizarin red staining was performed on days 7, 14 and 21 of differentiation. (**d**) The MTT test was conducted at 24, 48, and 72 h). Spindle-shaped fibroblast-like morphology and MSC-like surface markers, including CD90, and CD105 were exhibited by hEnMSCs. Hyb-1 scaffold revealed the highest calcium deposition (as an index of osteogenic differentiation) and cell viability. Statistical significance is indicated as follows: ***$P < 0.001$, ** $P < 0.01$, and * $P < 0.05$. Data are presented as mean ± SD ($n = 3$)

Additional experiments were carried out to evaluate calcium deposition (in 7, 14, and 21 days) and cell viability (24, 48 and 72 h). The results of indirect alizarin red staining, conducted using the scaffold extract-enriched culture medium on hEnMSCs, revealed greater calcium deposition in the Hyb-1 sample when compared to the other two samples in all time intervals (Fig. 5c). Furthermore, the MTT assay results indicated that hEnMSCs survival was lower in the Hyb-2 group compared to the PCL-nHA and Hyb-1 groups (Fig. 5d). These findings confirm the enhanced interaction between hEnMSCs and natural polymers. Based on these compelling results, Hyb-1 scaffolds, which exhibited increased porosity and interconnected pores, were selected for subsequent drug loading, release studies, and in vitro evaluations.

Exploring in vitro osteogenic differentiation

In this research, we examined how a scaffold with DEX-loaded microparticles, designed for the controlled release of DEX, affects the differentiation of hEnMSCs into osteoblasts, in comparison to scaffolds unloaded with DEX.

Gene expression analysis

To assess the osteoblastic differentiation of hEnMSCs, gene expression analysis was conducted to examine the levels of key osteogenic genes, including COL1A1, OST, and RUNX2, on days 14 and 21 (Fig. 6a-c). The expression levels of COL1A1 and OST were significantly higher in the Hyb-1-DEX group compared to the other groups at both 14 and 21 days, indicating enhanced matrix

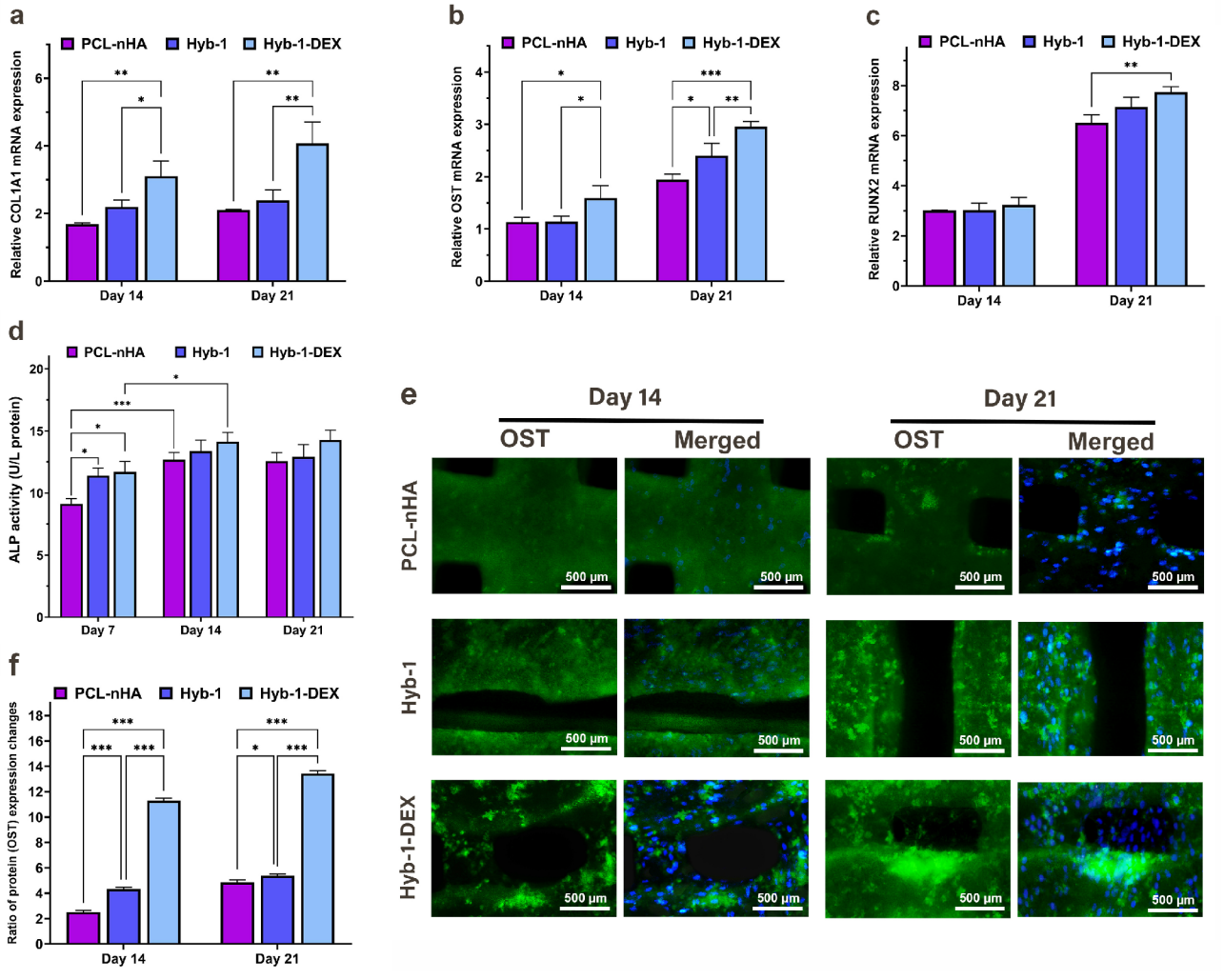

Fig. 6 Osteogenic Differentiation of hEnMSCs. Gene expression analysis of (**a**) collagen one, (**b**) osteonectin, and (**c**) RUNX2 on days 14 and 21 of differentiation. (**d**) Alkaline Phosphatase (ALP) activity measured on days 7, 14, and 21 of differentiation. DEX enhanced the expression of all osteogenic genes, however, its effect on COL1A1 and OST is more obvious. (**e**) Immunocytochemical staining of osteonectin at 14 and 21 days after differentiation. (**f**) Quantitative graph depicting the ratio of osteonectin protein expression in the samples. DAPI-stained cell nuclei are shown as blue dots, while osteonectin protein is represented by light green spots. Hyb-1-DEX revealed intense and extensive green fluorescence compared to Hyb-1, and PCL-nHA in both time intervals. ***$P < 0.001$ **$P < 0.01$ *$P < 0.05$

synthesis and deposition in the presence of the DEX-MPs. These findings suggest that the controlled release of DEX influenced the differentiation process, leading to increased expression of genes associated with bone formation. Statistically significant differences were denoted by asterisks: $^{*}p < 0.05$, $^{**}p < 0.01$, and $^{***}p < 0.001$.

Additionally, the expression of RUNX2, a master regulator of osteoblast differentiation, was significantly higher than the other examined genes at both time points across all groups. This highlights the crucial role of RUNX2 in the orchestration of osteoblast differentiation. Moreover, on day 21, the expression level of RUNX2 in the Hyb-1-DEX group was significantly higher compared to the PCL-nHA group ($p < 0.001$). However, there was no statistically significant difference in RUNX2 expression between the groups on day 14, suggesting that factors beyond RUNX2 may contribute to the observed differentiation effects induced by the DEX-MPs.

ALP assay

The alkaline phosphatase (ALP) activity was assessed on days 7, 14, and 21 post-seeding of hEnMSCs on the scaffolds (Fig. 6d). On the 7th day, the Hyb-1-DEX group showed significantly higher ALP activity compared to the PCL-nHA group ($p < 0.05$). However, there was no significant difference in ALP activity between the Hyb-1-DEX group and the Hyb-1 group. On the 14th day, no significant differences in ALP activity were observed among the three groups. Notably, ALP activity increased from day 7 to day 14 in all groups, with significant increases observed in the Hyb-1-DEX and PCL-nHA groups ($p < 0.05$ and $p < 0.001$, respectively), indicating continuous osteogenic differentiation. By the 21st day, there were no significant differences in ALP activity among the three groups. ALP activity levels remained relatively consistent from day 14 to day 21, showing no significant variations within the groups.

Quantification and visualization of osteonectin expression

The cellular localization and expression patterns of osteogenic secreted protein (OST) were analyzed using immunocytochemistry (ICC) on days 14 and 21 for the three experimental groups. Immunofluorescence staining displayed green fluorescence from the OST antibody and blue fluorescence from cell nucleus staining (Fig. 6e-f). It was observed that the distribution of the OST marker was wider on day 21 compared to day 14 in all groups. Particularly, the Hyb-1-DEX group exhibited intense and extensive green fluorescence compared to the other two groups on both the 14th and 21st days. The staining area was quantified using ImageJ software to determine the relative amount of OST. The quantitative results, in line with gene expression data, demonstrated significantly higher levels of OST in the Hyb-1-DEX scaffold group compared to both control groups on both day 14 and day 21 ($p < 0.001$). These findings indicate that the incorporation of DEX-MPs into Hyb-1 scaffolds significantly enhances the secretion of OST protein in comparison to PCL-nHA and Hyb-1 scaffolds.

Visualization and assessment of calcium accumulation

Cell attachments, cytotoxicity assessment and alizarin red staining of scaffolds (PCL-nHA, Hyb-1, Hyb-1-DEX) were presented in Fig. 7. Cell attachment to scaffolds (PCL-nHA, Hyb-1, Hyb-1-DEX) was evaluated by SEM images of hEnMSCs cultured on them at day 5 at different magnifications (Fig. 7a). These images clearly illustrate that all scaffold types facilitate robust cell adhesion, indicating their non-toxicity and excellent biocompatibility. Notably, within the Hyb-1-DEX group, hEnMSCs displayed a higher degree of proliferation and more active distribution, establishing stronger cell-to-cell connections. This observation suggests that the controlled release of DEX in the initial days following cell seeding on the scaffolds played a highly effective and stimulatory role in promoting hEnMSCs growth and adhesion. Also, the results from the MTT assay demonstrate a consistent upward trend in cell survival rates up to the fifth day across all experimental groups. A noteworthy discovery in this investigation pertains to the notably higher cell survival rates observed in the Hyb-1-DEX group in comparison to the other two groups. On the first and third day after cell seeding, hEnMSCs exhibited effective growth in all scaffold groups, but Hyb-1-DEX scaffolds displayed a significantly higher level of cell proliferation compared to the other two groups ($p < 0.001$) (Fig. 7b). Similarly, by the fifth day, the Hyb-1-DEX scaffolds exhibited significantly higher cell proliferation and viability compared to the PCL-nHA ($p < 0.001$) and Hyb-1 samples ($p < 0.05$). These outcomes validate the strong biocompatibility of all scaffold groups, with particular emphasis on the hybrid-DEX group.

Moreover, to evaluate mineralization within the scaffolds seeded with hEnMSCs, an ARs test was conducted in both qualitative and quantitative moods on days 14 and 21 (Fig. 7c-d). Quantitative analysis involved measuring absorbance at 405 nm, which demonstrated a statistically significant increase in mineralization in the Hyb-1-DEX group compared to the Hyb-1 group on both days 14 and 21 ($p < 0.05$ and $p < 0.01$, respectively). Additionally, the Hyb-1-DEX group exhibited significantly higher mineralization compared to the PCL-nHA group ($p < 0.001$). These results provide compelling evidence of the substantial impact of sustained dexamethasone release on promoting bone formation and subsequent mineralization of the extracellular matrix.

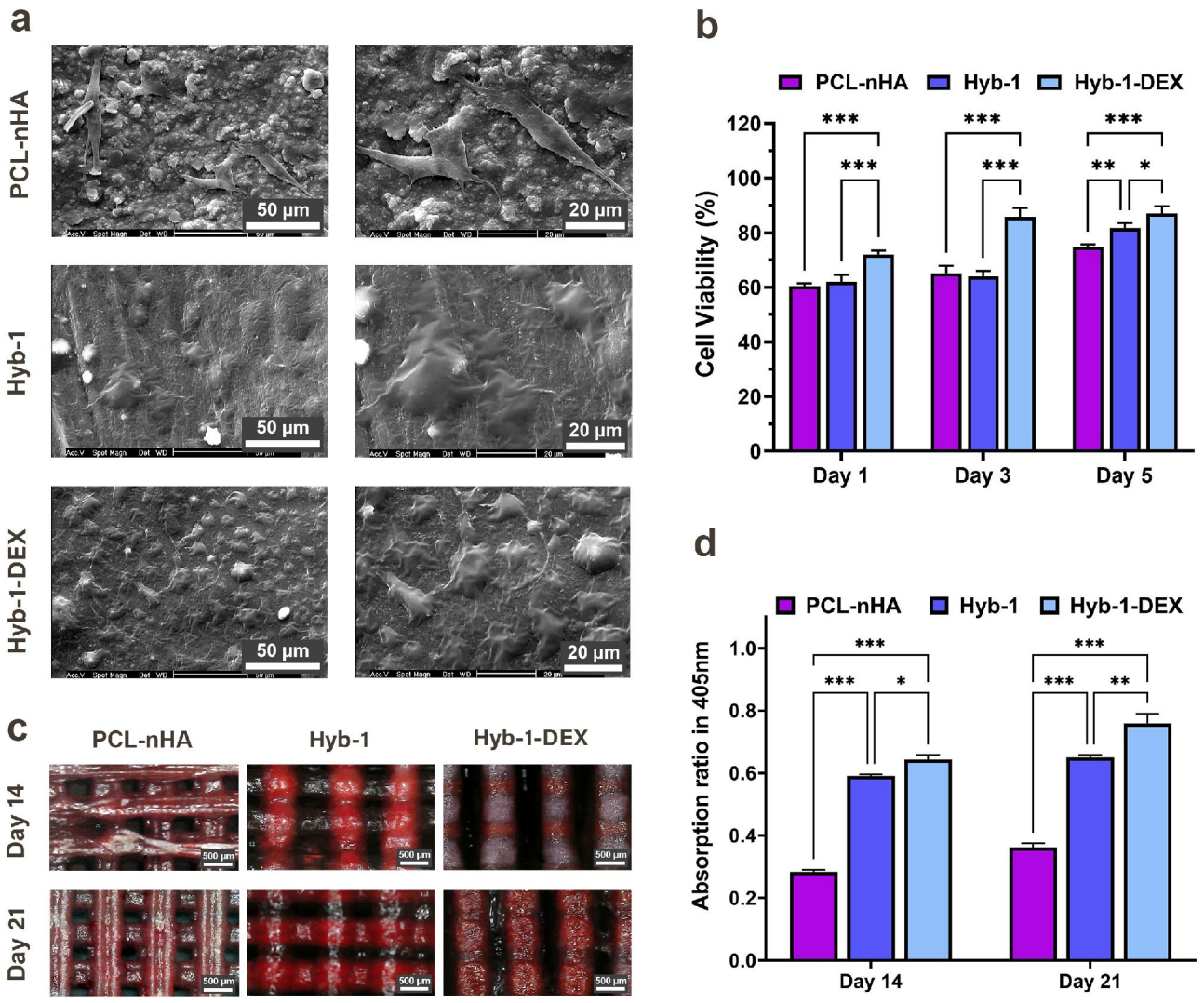

Fig. 7 Scaffolds cell attachments, cytotoxicity assessment and alizarin red staining on days 14 and 21 of differentiation for PCL-nHA, Hyb-1, and Hyb-1-DEX groups. (**a**) SEM images depicting hEnMSCs cultured on scaffolds, at different magnifications on day 5. (**b**) MTT assay results assessing hEnMSCs survival and proliferation on 3D printed scaffolds on days 1, 3, and 5 days. (**c**) Visual representation, and (**d**) Quantitative color analysis of alizarin red staining for PCL-nHA, Hyb-1, and Hyb-1-DEX scaffolds on days 14 and 21 of differentiation (scale bar = 500 µm). Hyb-1-DEX scaffolds induced higher proliferation and osteogenic differentiation in hEnMSCs in both time intervals. *** $P < 0.001$ level. ** $P < 0.01$ level. * $P < 0.05$ level

Discussion

Over than 14 million people in the United States (US), and more than 200 million people globally have osteoporosis, a condition characterized by reduced bone mineral density. The primary causes of bone loss include obesity, genetic disorders, accidents, and aging [98]. While autografts are the standard treatment for bone injuries, their use is limited due to accessibility and risks. As a result, new approaches such as tissue engineering are gaining traction in bone repair. Tissue engineering focuses on creating scaffolds to support bone cells and promote the regeneration of bone tissue [99]. From a histological point of view, bone tissue is a natural mixture of bioceramic and polymeric phases, mainly apatite and collagen [100].

Hence, scaffolds which consist of organic-inorganic hybrid polymeric composites containing hydroxyapatite nanoparticles, show promise for bone tissue engineering. Specifically, 3D-printed porous polymer nanocomposite scaffolds, including those made from polycaprolactone, are suitable for supporting various types of cells due to their mechanical properties, cost-effectiveness, biocompatibility, and printability [101, 102]. Moreover, recent approaches in bone tissue engineering focus on creating biomimetic scaffolds using hydrogels, such as alginate-gelatin, to induce biomineralization and drug delivery [103]. Sustained release of drugs, including microcarriers and nanocarriers, has been shown to support tissue healing [104]. Amongst, Dexamethasone, a drug for inducing bone differentiation, has been used in microparticles

within the scaffold structure [105]. The current study involves fabricating biomimetic nanocomposite scaffolds with sustained drug release using 3D printing, optimizing for biological and mechanical performance to promote osteogenesis in endometrial mesenchymal stem cells. The development of hybrid systems, combining osteoinductive 3D-printed scaffolds and cell-laden hydrogels, has shown great potential for bone tissue engineering and the treatment of bone defects based on active tissue regeneration.

Basically, the main aim of the study was to develop hybrid scaffolds with sustained release of DEX, which mimicked the extracellular matrix (ECM) while enhancing the differentiation potential of hEnMSCs into osteoblasts, thus facilitating bone regeneration. One of the key aspects of this study was the similarity of the hybrid scaffolds, composed of nHA, gelatin, and alginate, to the ECM of bone tissue which promotes osteoconductivity and creates a biomimetic microenvironment. Given the self-renewal nature of MSCs and their inherent potential for osteogenic differentiation [106], these scaffolds have proven effective in enhancing hEnMSCs adhesion, migration, proliferation, and ultimately, bone formation by guiding the behavior of MSCs.

The homogenous incorporation of DEX-MPs within the hydrogel, entrapped in the hybrid scaffolds, allowed precise control over sustained drug release (Fig. 3). Furthermore, the use of 3D printing technology played a pivotal role in designing the hybrid scaffolds as it provided precise control over dimensions, structure, and porosity, ensuring optimal structural integrity (Fig. 2). These scaffolds exhibited favorable mechanical properties, ensuring sufficient stability and support for hEnMSCs colonization and osteogenesis. By combining the structural, mechanical, and bioactive properties of the hybrid scaffolds with controlled release of DEX, a synergistic approach for BTE was sought to be achieved.

Overview data of (Table 2) demonstrated that increasing the initial DEX percentage compared to the polymer led to a corresponding rise in DEX encapsulation within the MPs. This trend could be explained by considering that the drug content in these MPs is influenced by the interactions between the drug and polymer, with higher drug mixing resulting in greater drug incorporation [107]. Furthermore, the percentage of drug loading closely mirrors the initial drug concentration applied during fabrication. This suggests that, regardless of the initial drug concentration, a significant amount of drug is consistently loaded into the MPs. In this study, encapsulation and drug loading efficiencies of DEX align with previous reports [75, 82].

Also, the results from DLS indicate that the size of microparticles increases with higher initial drug concentrations. Given that only a fixed amount of drug can be accommodated within a specific quantity of polymer, the increased drug content leads to a more viscous dispersed phase, which in turn, contributes to larger microparticle dimensions [107]. Notably, the particle size distribution falls within the range of 0.24 to 5.58 µm (Fig. 1b), which is consistent with similar studies and is well-suited for the intended application of controlled drug release [74]. Moreover, FESEM images (Fig. 1a) reveal the smooth and uniform morphology of the MPs, consistent with the DLS results (Fig. 1b). These visual observations affirm the successful fabrication of MPs with the desired properties, reinforcing their potential for controlled drug release applications.

The zeta potential, a measure of surface charge, illustrates that drug-free MPs exhibit a zeta potential of -27.7, while drug-containing microparticles display a more negative value of approximately – 31.56 (Fig. 1c). This change can be attributed to the presence of the drug within the microparticles. Zeta potential values within the range of -15 to -30 mV are considered ideal for stabilizing microparticles [108, 109]. The negative charge plays a crucial role in preventing microparticle aggregation, maintaining their dispersed state, and ensuring the stability of the microparticle system, which are essential factors for controlled drug release and targeted delivery to hEnMSCs [110].

In this study, we successfully fabricated hybrid scaffolds with integrated and coherent structure using a layer-by-layer approach, which included Alg-Gel and PCL-nHA composites. Calcium chloride (CaCl2) and glutaraldehyde were applied as crosslinkers after each Alg-Gel layer printing and after the completion of the complete 3D scaffold printing. In a general sense, the polyanionic carboxylate groups (-COO^-) in alginate [111] and the polycationic amine groups (NH2-) in gelatin [112] can potentially form weak electrostatic interactions between the two materials [88]. Simultaneously, the Ca^{2+} ions present in the $CaCl_2$ solution infiltrate the alginate matrix, leading to an ion exchange with Na^+ ions. This process facilitates the formation of ionic bridges between alginate's carboxylate groups (-COO^-) and the formation of a gel network [111]. This gelation process results in the creation of a coherent and stable structure of Alg-Gel, onto which the layer of PCL-nHA can be easily placed. Moreover, glutaraldehyde, with its aldehyde functional groups (-CHO), forms covalent imine bonds (C = N) with the amine groups (-NH2) of gelatin [113], thereby enhancing the structural integrity.

Additionally, there may be cross-links between the -OH group of nHA and the -CHO of glutaraldehyde [114]. Previous studies have also proved interactions between the phosphate functional groups (-PO_4^{3-}) and Ca^{2+} ions in hydroxyapatite and the carboxyl and amine functional groups of gelatin-chitosan-alginate when combining

these materials [114–116]. These findings support the hypothesis that interactions between calcium ions, phosphate groups, and carboxyl/amine groups within hydroxyapatite, gelatin, and alginate contribute to scaffold stability. However, the precise mechanisms underlying this phenomenon remain unclear. Furthermore, the textured and porous surface of the PCL-nHA composite layers allows for the penetration and interlocking of Alg-Gel layers. These physical interactions contribute to the mechanical stability and strong interface between the layers. Further research is still needed to fully elucidate the specific mechanisms and extent of these interactions.

SEM images (Fig. 2) revealed scaffold shrinkage following freeze-drying. This shrinkage varied among scaffold types, likely due to a combination of material properties, solvent type, and inter-component interactions. Alg-Gel scaffolds exhibited the highest shrinkage (35.99 ± 2.09%), potentially reflecting the hydrogel's susceptibility to deformation during the drying process. In contrast, PCL-nHA scaffolds showed minimal shrinkage (5.37 ± 0.677%), possibly attributed to strong interactions between PCL and nHA [117] that maintained scaffold structural integrity. The substantial difference in shrinkage may also be linked to the solvents employed. DCM, a volatile organic compound (VOC) used for PCL, evaporates rapidly during 3D printing and drying [118], whereas water, used for the alginate and gelatin in Alg-Gel scaffolds [119], evaporates more slowly. The higher water content in Alg-Gel inks (resulting from a higher solvent-to-material ratio in ink preparation—see Methods section), combined with the hydrophilicity of alginate and gelatin [120], likely led to greater water loss and consequently higher shrinkage during drying [121]. This observation aligns with findings reported in other studies [121, 122].

Hyb-1 and Hyb-2 scaffolds, containing both PCL-nHA and Alg-Gel components, exhibited moderate shrinkage. Hyb-2 (9.93 ± 1.95% shrinkage) showed less shrinkage than Hyb-1 (14.07 ± 2.53%), likely due to differences in Alg-Gel distribution. In Hyb-2, Alg-Gel filaments were less numerous and more dispersed, between PCL-nHA filaments which provided greater structural support and reduced the Alg-Gel's contribution to overall shrinkage compared to Hyb-1, where Alg-Gel and PCL-nHA layers are stacked.

Hyb-1 scaffolds exhibited pore size changes in addition to overall shrinkage. However, the scaffold's overall dimensions remained largely unchanged due to interlayer crosslinking and the structural support provided by the PCL-nHA component. Subsequent immersion in aqueous media resulted in hydrogel swelling and pore size recovery to near-original dimensions, consistent with the findings of Luo Y et al. [121].

The change in pore dimensions in the Hyb-1 scaffold after drying and rehydration can be attributed to the different swelling properties of the PCL-nHA and Alg-Gel components. Drying resulted in greater Alg-Gel shrinkage than PCL-nHA shrinkage, leading to elongated pores. The observed variations in scaffold shrinkage and pore dimensions are likely due to the different solvents, rehydration, and swelling properties of the PCL-nHA and Alg-Gel components.

Previous studies conducted degradation tests within a timeframe of less than 30 days [76, 123, 124]. The present study was monitored scaffold degradation over a period of 12 weeks (Fig. 3a). Dorj et al. investigated the degradation rate of PCL-HA scaffolds with a 40:60 ratio using acetone and tetrahydrofuran (THF) solvent, which resulted in approximately 6% degradation after 14 days [123]. In our study, this composite achieved a similar degradation level after 12 weeks, indicating a slower degradation rate. Additionally, other studies assessed the degradation of PCL-13-93B3 composite with a 50:50 ratio in chloroform solvent, revealing a degradation rate of about 30% after 2 and 4 weeks [76, 124, 125]. Our study demonstrated that as the content of Alg-Gel hydrogel increased in the overall scaffold structure, the degradation rate increased. Due to their natural composition, hydrophilic nature, and weaker chemical bonds, Alg-Gel scaffolds are more susceptible to enzymatic decomposition, hydrolysis, and swelling, resulting in a higher degradation rate. This makes them suitable for drug delivery systems that require rapid degradation [40]. Similar research conducted by Kolan et al. evaluated hybrid scaffolds PCL-13-93B3 and Pluronic F127 hydrophilic and temperature-sensitive hydrogel. Their study reported a degradation rate of 20% after one week [77], whereas in our study, at the same time, Hyb-1 and Hyb-2 scaffolds exhibited degradation rates of only 2.5 ± 0.63 and 2.2 ± 0.68, respectively. Another study investigating the degradation behavior of PCL-GelMA hybrid scaffolds reported a degradation rate of 2% after three weeks [126], which corresponds with our findings for Hyb-1 (5.08 ± 0.35) and Hyb-2 (2.7 ± 0.62) after three weeks. As a result, the choice of solvent and temperature, material type and percentage, interactions and cross-linking characteristics, material distribution, presence of impurities, and scaffold design and layering can all influence the physicochemical properties of the scaffold, including the degradation rate [127, 128].

Moreover, the combination of PCL and nHA in the scaffold provided structural integrity and biocompatibility, while the addition of Alg-Gel improved mechanical performance. The PCL-nHA scaffolds exhibited brittle behavior, whereas the Hyb-1 scaffold with the inclusion of Alg-Gel showed advantages in terms of deformation capacity and stress distribution [129]. The hydrogels contributed to increased toughness and energy absorption, enabling the scaffold to withstand higher compressive

loads without failure [130], as evidenced by the highest strain at failure (Fig. 3d). Although, the mechanical behavior of the Hyb-2 scaffold was slightly higher than Hyb-1, particularly the higher strength observed in Hyb-2, are relevant to lower Alg-Gel content, this study mainly emphasized investigating the biological efficiency of scaffolds on osteogenesis. Therefore, the Hyb-1 scaffold was chosen for drug loading and osteogenesis assays due to its higher cell interaction, porosity, and promising preliminary results in osteogenic differentiation.

Additionally, it can be claimed that the presence of Alg-Gel in the scaffold structure particularly in Hyb-1 scaffolds, can mimic the role of collagen as a soft phase in bone structure which leads to outstanding toughness of bone [128].

Overall, this study underscores the significance of meticulous material selection, optimization, and scaffold design in achieving desired mechanical properties for BTE. Processing parameters, such as solvent choice, temperature, material percentage, and interactions between composite components, can significantly influence the physicochemical properties and degradation rate of the scaffold. Thus, the combination of PCL-HA and Alg-Gel composites presents a promising approach for constructing scaffolds with favorable mechanical behaviors for bone regeneration and drug delivery purposes.

The results of the release curves fitting with mathematical models showed different release kinetics for free MPs (MPs-DEX) and the MPs-DEX entrapped in the Hyb-1 (Hyb-1-MPs-DEX) (see **Table 4**). The release of DEX from the free MPs follows a primarily Fickian diffusion-controlled pattern with a high release rate, whereas the release from the Hyb-1 scaffolds exhibits a non-Fickian Super Case-II transport mechanism dominated by polymer relaxation and degradation, showing a slower and potentially more controlled release [97]. The structural components of the Hyb-1 matrix seem to be involved in sustained DEX release [97]. This drug-release kinetic model has also been previously reported in systems consisting of hydrogels [131, 132]. The release rate constants were also lower for Hyb-1-MPs-DEX in comparison with MPs-DEX, indicating a reduced release rate for the Hyb-1 scaffold system. The MPs-DEX do not present any physical barrier to diffusion, contrary to the porous structure of the Hyb-1, in which the drug needs to diffuse through an additional barrier in addition to the MPs itself.

The slow and sustained release profiles observed from the scaffold-encapsulated microparticles hold promise for controlled drug delivery. Sustained release allows long-term drug availability, improving therapeutic efficacy and reducing dosing frequency [133]. The initial burst release is due to weakly attached DEX molecules on the microparticle surface or poorly encapsulated regions in the scaffold [134]. This burst release is reduced in scaffold-encapsulated microparticles compared to free MPs, thanks to an additional diffusion barrier created by the hybrid scaffold matrix.

Interestingly, we observed a strong correlation between the DEX release and the in vitro degradation profiles of the Hyb-1 (Fig. 3). The degradation test showed a slow weight loss during the first 3 weeks, after which the degradation rate accelerated. Similarly, the initial stage and then the gradual increase in drug release from days 16 to 30 align with the degradation pattern of Hyb-1 (Fig. 3). This strong correlation suggests that scaffold degradation plays a crucial role in controlling the drug release from Hyb-1. The initial slow release may be attributed to the low initial degradation and the need for the drug to diffuse through the matrix. The increased degradation rate of Hyb-1 creates larger pores [131], causing incorporated MPs to lose their structural support, which in turn facilitates the release of more microparticles and dexamethasone. Changes in hydrogel cross-linking density and dexamethasone diffusion characteristics contribute to this phenomenon [135]. This is consistent with the zero-order fit, which suggests that the DEX release rate is approximately constant after an initial phase that overcomes the immediate-release first-order systems and results in long-term maintenance of drug concentrations in the therapeutic range [95]. The release mechanism is thus influenced by a combination of polymer erosion, and possibly diffusion with zero-order model. So if initially the release mechanism may be accompanied by diffusion, matrix degradation becomes the rate-limiting factor. Overall, both polymer relaxation, as suggested by the Korsmeyer-Peppas model, and subsequent matrix degradation contribute to the sustained and non-Fickian release of DEX in Hyb-1.

In the scaffold-entrapped DEX-MPs, we observed an initial burst release of about 2 µg, followed by a slower, more uniform release. This controlled release can inhibit inflammatory reactions in the first days since a concentration of DEX between 0.5 and 5 µg/ml is known to inhibit the inflammatory response of macrophages [136]. In previous studies, the effective dose of DEX for osteogenic differentiation has been reported between 4 and 400 ng/ml [137–139]. In our study, the average drug release from day 1 to day 16 was approximately 133 ng from each scaffold, providing insights into drug release kinetics relevant to bone differentiation, and biomineralization (Fig. 3f). Sustained release of DEX from scaffold-entrapped DEX-MPs, especially in the effective concentration range, benefits osteogenic differentiation, demonstrating successful drug delivery for BTE applications [25, 140, 141].

The evaluation of osteogenic differentiation, using gene expression analysis of RUNX2, COL1A1, and OST at days 14 and 21, revealed a complex interplay between

DEX-MPs, the biomaterial properties of the scaffold, and intrinsic cellular responses. In line with previous research, our study demonstrates that scaffolds containing controlled-release DEX-MPs enhance the differentiation of hEnMSCs into osteoblasts compared to scaffolds without the DEX [136, 142, 143]. Gene expression analysis revealed significant upregulation of COL1A1 and OST, key markers of late-stage osteoblast differentiation and matrix maturation [144], in the Hyb-1-DEX compared to Hyb-1 and PCL-nHA on days 14 and 21, confirming the beneficial effect of the DEX release system on osteoblast activity and bone formation (Fig. 6). These findings align with our visual and quantitative assessments from the ICC test, which reveal stronger and more extensive green fluorescence in the Hyb-1-DEX, in comparison to both PCL-nHA and Hyb-1 on days 14 and 21 (Fig. 6e). Moreover, the higher level of OST protein in the Hyb-1, compared to the PCL-nHA, suggests that the natural polymer composition, along with HA, provides a conducive environment for promoting bone differentiation and facilitating increased expression of OST.

RUNX2, Known as a key transcription factor responsible for regulating osteoblast differentiation [145, 146], exhibited increased expression in all groups, highlighting its critical role in governing osteoblast differentiation. However, the absence of a significant difference in RUNX2 expression between the groups on day 14, and only a slight difference against PCL-nHA on day 21 ($p < 0.01$), suggests the involvement of additional factors that contribute to the observed differentiation effects caused by the DEX-MPs (Fig. 6c). This trend, which is that the presence of a component can significantly increase only one or two bone biomarkers but has no significant effect on the others, has also been seen in the work of other researchers [3]. This indicates that the DEX-MPs may primarily influence later stages of osteogenic differentiation, consistent with studies showing enhancement of downstream signaling pathways involved in ECM protein synthesis, rather than directly affecting the initial transcriptional activation mediated by RUNX2 [147–149]. Despite observed improvements in bone formation, the lack of a statistically significant difference in RUNX2 expression likely reflects the complex interplay of multiple factors influencing osteogenic differentiation. Firstly, the limitations in experimental design might not have fully captured the dynamic expression patterns of RUNX2, highlighting the need for future studies employing a more comprehensive temporal analysis. Secondly, the complexity of osteogenesis suggests compensatory mechanisms may be at play. While RUNX2 is a crucial transcription factor, bone formation is regulated through multiple interconnected pathways, such as TGF-β and Wnt signaling [148, 149]. The controlled release of DEX influences osteogenesis via diverse pathways, including the induction of mineralization, secretion of BMP2, and activation of the hedgehog pathway [25, 150–152]. Furthermore, DEX has been shown to stimulate osteoblast-derived extracellular vesicle secretion, promoting bone differentiation [153]. These alternatives signaling pathways could compensate for subtle changes in RUNX2 expression, resulting in enhanced bone formation despite the non-significant change in RUNX2 levels. Finally, inherent biological variability must also be considered, including intrinsic cellular heterogeneity, variations in MSC responsiveness to DEX, and the unique biophysical properties of scaffold and paracrine signaling within the 3D microenvironment [154–156]. Further research is necessary to fully elucidate the contribution of each of these factors to the observed effects and clarify the complex interplay between RUNX2 and other signaling pathways in the context of the controlled DEX release system.

The higher ALP activity in the Hyb-1-DEX compared to the two other groups over time, especially the significantly higher ALP activity on day 7 in the Hyb-1-DEX compared to the PCL-nHA ($p < 0.05$), can be partially attributed to the presence of the DEX-MPs within the scaffolds. However, the absence of significant differences between the Hyb-1-DEX and the other two groups on days 14 and 21 requires further analysis. Scaffold structural components, including alginate and gelatin, in both the Hyb-1-DEX and Hyb-1, may have influenced ALP activity [157–159]. The presence of these biopolymers in Hyb-1 likely mitigates the long-term impact of DEX, leading to similar ALP activity levels between groups by days 14 and 21. As shown in a study, the potential of chitosan addition to the culture medium for osteogenic differentiation of DPSCs was almost similar to that of DEX by evaluating markers such as ALP and RUNX-2 [160]. Also, in another study, Amjadian et al. did not observe a significant difference in ALP activity on day 7 in the PLLA, nHA, DEX/gelatin compared to the PLLA, nHA/gelatin [161]. Throughout the study period, ALP activity peaked on the 14th day. It remained relatively stable until the 21st day in all groups, indicating that the continuous release of DEX effectively supports and sustains osteogenic differentiation (Fig. 6d). This observation likely arises from the inherent temporal dynamics of ALP during osteoblast differentiation, where activity peaks around day 14 and subsequently plateaus, as seen in other studies [157, 162, 163]. This inherent biological process, combined with the osteoconductive properties of biopolymers, may obscure any difference in ALP activity beyond day 7 [157]. Also, the results of ARs support the conclusion that the Hyb-1-DEX scaffold enhances osteogenic potential, thereby promoting increased mineral matrix formation compared to the control groups (Fig. 4, **and** Fig. 7).

In summary, despite the lack of significant differences in RUNX2 expression and ALP activity between groups on days 14 and 21, the significant upregulation of COL1A1 and OST, coupled with improved ARs and ICC, strongly suggests that the Hyb-1-DEX effectively enhances osteogenic differentiation of hEnMSCs. Further research is needed to fully elucidate the specific contribution of each factor and the underlying mechanisms involved in this process.

While 3D bioprinting holds great promise for preclinical and clinical applications, significant challenges persist regarding the accuracy, printing speed, scalability, and reproducibility of bioprinters. At present, no single 3D bioprinter has been developed that outperforms all others across these key performance metrics [70, 164]. One limitation of the present study is the increased printing time due to the temporary pause required after each hydrogel layer extrusion to facilitate cross-linking. This pause was necessary to prevent structural collapse and ensure the successful printing of subsequent layers, but it extended the overall printing process. Future studies should explore alternative strategies to accelerate crosslinking without compromising the integrity of the printed constructs.

Also, despite the fact that hybrid nature of the designed scaffolds in this research can be considered an innovative biomimetic strategy for bone healing [165, 166]. However, there are still serious challenges that need to be addressed, such as enhancing adhesion and integrity, and limitations of using glutaraldehyde as crosslinker. Using a multifunctional crosslinker that can create chemical bonds between the different layers of the scaffold (Alg-Gel-MPs and PCL-nHA) could enhance the adhesion between the layers and boost the overall integrity of the scaffold. This could improve the load-bearing capacity and mechanical properties of the scaffold. In this research, as described, we used CaCl2 and glutaraldehyde as a well-known chemical crosslinkers that can create strong chemical bonds in Alg-Gel-MPs layers. While glutaraldehyde has been used for coating gelatin on PCL scaffolds, its ability to create chemical bonds between PCL and Gel by using glutaraldehyde has not been proven [167]. Subsequently, the potential toxicity of the crosslinker used to polymerized the hydrogel layers should be considered.

Consequently, this study emphasizes the significance of optimizing scaffold design, release kinetics, and drug concentration to enhance bone regeneration. The results demonstrate that incorporating DEX-MPs into the hydrogel and subsequently 3D printing it as hybrid scaffolds offers a controlled drug delivery system. This not only ensures the sustained presence of DEX but also potentially enhances the osteogenic potential of the Hyb-1-DEX group. Further research is required to comprehend the underlying mechanisms governing the release behavior and optimize the scaffold system for precise and targeted drug delivery. Future studies can focus on evaluating the degradation properties of the hydrogel, elucidating the drug release mechanisms within the matrix, conducting additional cellular assays, employing in vivo models, assessing the long-term effects of DEX on BTE, and exploring alternative crosslinkers.

Conclusion

In this research, we incorporated DEX-loaded PCL MPs uniformly into a hydrogel, which was then 3D printed to create layer-by-layer hybrid scaffolds. These scaffolds featured interlayers of PCL-nHA and Alg-Gel composites for bone regeneration. The hybrid scaffolds exhibited favorable mechanical stability, biocompatibility, and biodegradability, providing an ideal environment for the growth and proliferation of hEnMSCs. The integrated MPs-DEX into the hybrid scaffold demonstrated more controlled release of the DEX compared to free MPs-DEX, showing promise for sustained drug delivery. Moreover, the continuous release of DEX through Hyb-1-DEX scaffolds created a microenvironment conducive to activating bone signaling pathways, leading to enhanced bone differentiation and mineralization compared to PCL-nHA and Hyb-1 scaffolds. These findings were substantiated by significantly elevated expression levels of bone markers, including COL1A1 and OST, as well as the key transcription factor RUNX2. Increased ALP activity, as well as positive immunofluorescence staining for OST and ARs, further confirm the efficacy of the Hyb-1-DEX scaffolds. In conclusion, our innovative approach of 3D printing hybrid scaffolds with DEX-MPs presents a controlled drug delivery system that significantly boosts the osteogenic potential in BTE therapies.

Acknowledgments

The completion of this research paper would not have been possible without the support of Tehran University of Medical Science. I thank all the staff of School of Advanced Technologies in Medicine for their cooperation and kind support throughout my research period.

Author contributions

Parastoo Noory, Jafar Ai, and Jafar Ai are the principal investigators who formulated the study. The design of Figs. 1–11 involved contributions from Parastoo Noory, Shima Shojaie, Ali Farzin, Abdolreza Mohamadnia, and Mohammad Bayat. The biological analyses were conceptualized and overseen by Somayeh Ebrahimi-Barough, Abdolreza Mohamadnia, Arash Goodarzi, and Mohammad Bayat. Additionally, the characterization of materials was designed and supervised by Ahmad Reza Farmani and Ali Farzin. Data analysis, which included biological assessments and material characterizations, was conducted by Somayeh Ebrahimi-Barough, Naghmeh Bahrami, Ahmad Reza Farmani, and Arash Goodarzi. The primary manuscript text was drafted by Ahmad Reza Farmani and Parastoo Noory. The initial draft received editorial revisions from Jafar Ai, Naghmeh Bahrami, and Mohammad Bayat. The graphical abstract was created by Ahmad Reza Farmani and Hamed Hajmoradi. All authors reviewed the final manuscript version and provided their consent. All authors, particularly, Parastoo Noory, Ahmad Reza Farmani, Naghmeh Bahrami, and Jafar Ai prepared the revised manuscript.

Funding
This research was made possible through financial support from School of Advanced Technologies in Medicine, Tehran University of Medical Sciences (Grant Number 99-2-148-49468).

Data availability
No datasets were generated or analysed during the current study.

Declarations

Ethics approval and consent to participate
hEnMSCs were isolated following the ethical guidelines of Tehran University of Medical Science, Iran (IR.TUMS.MEDICINE.REC.1399.201).

Consent to participate
The authors declare that they have completely consent to participation.

Consent for publication
The authors declare that they have completely consent to publication.

Competing interests
The authors declare no competing interests.

Author details
[1]Department of Tissue Engineering, School of Advanced Technologies in Medicine, Tehran University of Medical Sciences, Tehran, Iran
[2]Department of Tissue Engineering, School of Advanced Technologies in Medicine, Fasa University of Medical Sciences, Fasa, Iran
[3]Craniomaxillofacial Research Center, Tehran University of Medical Sciences, Tehran, Iran
[4]Material Engineering Department, Faculty of Engineering, Tarbiat Modares University, Tehran, Iran
[5]Faculty of Medicine, Tehran University of Medical Sciences, Tehran, Iran
[6]Department of Internal Medicine, School of Medicine, Kashan University of Medical Sciences, Kashan, Iran
[7]Department of Biotechnology, School of Advanced Technologies in Medicine, Shahid Beheshti University of Medical Sciences, Tehran, Iran
[8]Chronic Respiratory Diseases Research Center (CRDRC), National Research Institute of Tuberculosis and Lung Diseases (NRITLD), Shahid Beheshti University of Medical Sciences, Tehran, Iran

Received: 18 October 2024 / Accepted: 28 April 2025
Published online: 20 May 2025

References

1. Duda GN, et al. The decisive early phase of bone regeneration. Nat Rev Rheumatol. 2023;19(2):78–95.
2. Verrier S, et al. Tissue engineering and regenerative approaches to improving the healing of large bone defects. Eur Cell Mater. 2016;32:87–110.
3. Farmani AR, et al. Preparation and in vitro osteogenic evaluation of biomimetic hybrid nanocomposite scaffolds based on gelatin/plasma rich in growth factors (PRGF) and Lithium-Doped 45s5 bioactive glass nanoparticles. J Polym Environ. 2023;31(3):870–85.
4. Turnbull G, et al. 3D bioactive composite scaffolds for bone tissue engineering. Bioact Mater. 2018;3(3):278–314.
5. Sharma A, et al. A self-organising biomimetic collagen/nano-hydroxyapatite-glycosaminoglycan scaffold for spinal fusion. J Mater Sci. 2017;52(21):12574–92.
6. Antebi B, et al. Controlling arteriogenesis and mast cells are central to bioengineering solutions for critical bone defect repair using allografts. Bioengineering. 2016;3(1):6.
7. Qi J, et al. Current biomaterial-based bone tissue engineering and translational medicine. Int J Mol Sci. 2021;22(19):10233.
8. Koushik TM, Miller CM, Antunes E. Bone tissue engineering scaffolds: function of Multi-Material hierarchically structured scaffolds. Adv Healthc Mater. 2023;12:2202766.
9. Walmsley GG, et al. Stem cells in bone regeneration. Stem Cell Reviews Rep. 2016;12:524–9.
10. Giannone G, et al. Endometrial cancer stem cells: role, characterization and therapeutic implications. Cancers. 2019;11(11):1820.
11. Cousins FL, Gargett CE. Endometrial stem/progenitor cells and their role in the pathogenesis of endometriosis. Volume 50. Best practice & research Clinical obstetrics & gynaecology; 2018. pp. 27–38.
12. Tanbo T, Fedorcsak P. Endometriosis-associated infertility: aspects of pathophysiological mechanisms and treatment options. Acta Obstet Gynecol Scand. 2017;96(6):659–67.
13. Mahdavinezhad F et al. The potential relationship between different human female reproductive disorders and sperm quality in female genital tract. Reproduct Sci. 2021;29:1–16.
14. Chaudhary A, Raza SS, Haque R. *Transcriptional factors targeting In cancer stem cells for tumor modulation*. In *Seminars In Cancer biology*. Elsevier; 2023.
15. Mobahat M, et al. Curcumin-loaded human endometrial stem cells derived exosomes as an effective carrier to suppress alpha-synuclein aggregates in 6OHDA-induced Parkinson's disease mouse model. Cell Tissue Banking. 2023;24(1):75–91.
16. Ebrahimi L, et al. Metformin-Loaded PCL/PVA fibrous scaffold preseeded with human endometrial stem cells for effective guided bone regeneration membranes. ACS Biomaterials Sci Eng. 2021;7(1):222–31.
17. Subbiah R, et al. Engineering of an osteoinductive and growth Factor-Free injectable bone-Like microgel for bone regeneration. Adv Healthc Mater. 2023;12(11):2200976.
18. Farmani AR, et al. Application of platelet rich fibrin in tissue engineering: focus on bone regeneration. Platelets. 2021;32(2):183–8.
19. Kowalczewski CJ, Saul JM. Biomaterials for the delivery of growth factors and other therapeutic agents in tissue engineering approaches to bone regeneration. Frontiers in Pharmacology; 2018. p. 9.
20. V KA, et al. Dual drug delivery platforms for bone tissue engineering. Front Bioeng Biotechnol. 2022;10:969843.
21. Madamsetty VS, et al. Dexamethasone: insights into Pharmacological aspects, therapeutic mechanisms, and delivery systems. ACS Biomaterials Sci Eng. 2022;8(5):1763–90.
22. Channey HS et al. Dexamethasone release pattern via a three-dimensional system for effective bone regeneration. Biomed Mater, 2023. 18(4).
23. Costa PF, et al. Additive manufacturing of scaffolds with dexamethasone controlled release for enhanced bone regeneration. Int J Pharm. 2015;496(2):541–50.
24. Chauhan N, et al. Dexamethasone-loaded, injectable pullulan-poly(ethylene glycol) hydrogels for bone tissue regeneration in chronic inflammatory conditions. Mater Sci Engineering: C. 2021;130:112463.
25. Majrashi M, et al. Sustained release of dexamethasone from 3D-Printed scaffolds modulates macrophage activation and enhances osteogenic differentiation. ACS Appl Mater Interfaces. 2023;15(49):56623–38.
26. Mansour A et al. Drug delivery systems in regenerative medicine: an updated review. Pharmaceutics, 2023. 15(2).
27. Abpeikar Z, et al. Development of meniscus cartilage using Polycaprolactone and decellularized meniscus surface modified by gelatin, hyaluronic acid biomacromolecules: A rabbit model. Int J Biol Macromol. 2022;213:498–515.
28. Abpeikar Z, et al. Characterization of macroporous Polycaprolactone/silk fibroin/gelatin/ascorbic acid composite scaffolds and in vivo results in a rabbit model for meniscus cartilage repair. Cartilage. 2021;13(2suppl):S1583–601.
29. Behl A, et al. Biodegradable Diblock copolymeric PEG-PCL nanoparticles: synthesis, characterization and applications as anticancer drug delivery agents. Polymer. 2020;207:122901.
30. Osanloo M, et al. The wound healing effect of polycaprolactone-chitosan scaffold coated with a gel containing Zataria multiflora Boiss. Volatile oil nanoemulsions. BMC Complement Med Ther. 2024;24(1):56.
31. Noori F, et al. Fabrication, characterization, and in vivo implantation of eugenol-loaded nanogels and PCL/Cs electrospun nanofibers for wound healing applications. J Bioactive Compatible Polym. 2023;38(6):480–92.
32. Luciani A, et al. PCL microspheres based functional scaffolds by bottom-up approach with predefined microstructural properties and release profiles. Biomaterials. 2008;29(36):4800–7.
33. Mahmoud BS, McConville C. Development and optimization of Irinotecan-Loaded PCL nanoparticles and their cytotoxicity against primary High-Grade glioma cells. Pharmaceutics, 2021. 13(4).
34. Pan Q, et al. Tumor-targeting Polycaprolactone nanoparticles with codelivery of Paclitaxel and IR780 for combinational therapy of drug-resistant ovarian cancer. ACS Biomaterials Sci Eng. 2020;6(4):2175–85.
35. Bai L et al. Hydrogel drug delivery systems for bone regeneration. Pharmaceutics, 2023. 15(5).

36. Carrêlo H et al. Injectable composite systems based on microparticles in hydrogels for bioactive cargo controlled delivery. Gels, 2021. 7(3).
37. Zhao F et al. Biomimetic hydrogels as the inductive endochondral ossification template for promoting bone regeneration. Adv Healthc Mater. 2023;13:2303532.
38. Farshidfar N, Iravani S, Varma RS. Alginate-Based biomaterials in tissue engineering and regenerative medicine. Mar Drugs, 2023. 21(3).
39. Sonaye SY, et al. Extrusion 3D (Bio)Printing of Alginate-Gelatin-Based composite scaffolds for skeletal muscle tissue engineering. Materials. 2022;15(22):7945.
40. Di Giuseppe M, et al. Mechanical behaviour of alginate-gelatin hydrogels for 3D Bioprinting. J Mech Behav Biomed Mater. 2018;79:150–7.
41. Mirek A, et al. Development of a new 3D bioprinted antibiotic delivery system based on a cross-linked gelatin–alginate hydrogel. J Mater Chem B. 2022;10(43):8862–74.
42. Poldervaart MT, et al. Sustained release of BMP-2 in bioprinted alginate for osteogenicity in mice and rats. PLoS ONE. 2013;8(8):e72610.
43. Sultan S, et al. The design of 3D-printed polylactic acid–bioglass composite scaffold: a potential implant material for bone tissue engineering. Molecules. 2022;27(21):7214.
44. Omigbodun FT, Oladapo BI. Enhanced mechanical properties and degradation control of Poly (Lactic) acid/hydroxyapatite/reduced graphene oxide composites for advanced bone tissue engineering application. Biomimetics. 2024;9(11):651.
45. Abdelaziz AG, et al. A review of 3D polymeric scaffolds for bone tissue engineering: principles, fabrication techniques, Immunomodulatory roles, and challenges. Bioengineering. 2023;10(2):204.
46. Zarei M, et al. Improving physio-mechanical and biological properties of 3D-printed PLA scaffolds via in-situ argon cold plasma treatment. Sci Rep. 2023;13(1):14120.
47. Fatemi A, Biglari FR. Microstructural and biological characterization of 3D printed PEEK scaffolds coated with alginate/cnt for bone regeneration applications. Discover Mech Eng. 2024;3(1):34.
48. Cho YS, Gwak S-J, Cho Y-S. Fabrication of Polycaprolactone/Nano hydroxyapatite (PCL/nHA) 3D scaffold with enhanced in vitro cell response via design for additive manufacturing (DfAM). Polymers. 2021;13(9):1394.
49. Gharibshahian M, et al. Recent advances on 3D-printed PCL-based composite scaffolds for bone tissue engineering. Front Bioeng Biotechnol. 2023;11:1168504.
50. Yuan X, et al. Recent advances in 3D printing of smart scaffolds for bone tissue engineering and regeneration. Adv Mater. 2024;36(34):2403641.
51. El-Rashidy AA, et al. Regenerating bone with bioactive glass scaffolds: A review of in vivo studies in bone defect models. Acta Biomater. 2017;62:1–28.
52. Ren X, et al. One-pot synthesis of hydroxyapatite hybrid Bioinks for digital light processing 3D printing in bone regeneration. Journal of Materials Science & Technology; 2024.
53. Farmani AR, et al. Li-Doped bioactive ceramics: promising biomaterials for tissue engineering and regenerative medicine. J Funct Biomaterials. 2022;13(4):162.
54. Farzin A, et al. A facile two step heat treatment strategy for development of bioceramic scaffolds for hard tissue engineering applications. Mater Sci Engineering: C. 2019;105:110009.
55. Saurav S, et al. Harnessing natural polymers for Nano-Scaffolds in bone tissue engineering: A comprehensive overview of bone disease treatment. Curr Issues Mol Biol. 2024;46(1):585–611.
56. Temple JP, et al. Engineering anatomically shaped vascularized bone grafts with hASCs and 3D-printed PCL scaffolds. J Biomedical Mater Res Part A. 2014;102(12):4317–25.
57. Far BF, et al. Synthesis and characterization of Chitosan/collagen/polycaprolactone hydrogel films with enhanced biocompatibility and hydrophilicity for artificial tendon applications. Int J Biol Macromol. 2023;127448:p.
58. Shor L, et al. Precision extruding deposition (PED) fabrication of Polycaprolactone (PCL) scaffolds for bone tissue engineering. Biofabrication. 2009;1(1):015003.
59. Yazdanpanah Z, et al. Printing tissue-engineered scaffolds made of Polycaprolactone and nano-hydroxyapatite with mechanical properties appropriate for trabecular bone substitutes. Biomed Eng Online. 2023;22(1):73.
60. Nyberg E, et al. Comparison of 3D-printed poly-ε-caprolactone scaffolds functionalized with tricalcium phosphate, hydroxyapatite, bio-oss, or decellularized bone matrix. Tissue Eng Part A. 2017;23(11–12):503–14.
61. Ronca D, et al. Bone tissue engineering: 3D PCL-based nanocomposite scaffolds with tailored properties. Procedia CIRP. 2016;49:51–4.
62. Lowe B, Hardy JG, Walsh LJ. Optimizing nanohydroxyapatite nanocomposites for bone tissue engineering. ACS Omega. 2020;5(1):1–9.
63. Liu L, et al. Homogeneous organic/inorganic hybrid scaffolds with high osteoinductive activity for bone tissue engineering. Polym Test. 2020;91:106798.
64. Collins MN, et al. Scaffold fabrication technologies and structure/function properties in bone tissue engineering. Adv Funct Mater. 2021;31(21):2010609.
65. Yazdanpanah Z et al. 3D bioprinted scaffolds for bone tissue engineering: State-Of-The-Art and emerging technologies. Front Bioeng Biotechnol. 2022;10.
66. Hosseini F, et al. 3D-printing-assisted synthesis of paclitaxel-loaded niosomes functionalized by cross-linked gelatin/alginate composite: Large-scale synthesis and in-vitro anti-cancer evaluation. Int J Biol Macromol. 2023;242:124697.
67. Zaer M, et al. Doxorubicin-loaded niosomes functionalized with gelatine and alginate as pH-responsive drug delivery system: A 3D printing approach. Int J Biol Macromol. 2023;253:126808.
68. Zhang Q, et al. Advanced biomaterials for repairing and reconstruction of mandibular defects. Mater Sci Engineering: C. 2019;103:109858.
69. Maroulakos M, et al. Applications of 3D printing on craniofacial bone repair: A systematic review. J Dent. 2019;80:1–14.
70. Bahraminasab M. Challenges on optimization of 3D-printed bone scaffolds. Biomed Eng Online. 2020;19(1):1–33.
71. Lin X et al. The bone extracellular matrix in bone formation and regeneration. Front Pharmacol. 2020;11.
72. Sahebalzamani M, et al. Advancing bone tissue engineering one layer at a time: a layer-by-layer assembly approach to 3D bone scaffold materials. Biomaterials Sci. 2022;10(11):2734–58.
73. Zhang S, Xing M, Li B. Biomimetic Layer-by-Layer Self-Assembly of nanofilms, nanocoatings, and 3D scaffolds for tissue engineering. Int J Mol Sci. 2018;19(6):1641.
74. Farzin A, et al. A facile way for development of three-dimensional localized drug delivery system for bone tissue engineering. Mater Sci Engineering: C. 2019;105:110032.
75. Balmayor ER, et al. Preparation and characterization of starch-poly-ε-caprolactone microparticles incorporating bioactive agents for drug delivery and tissue engineering applications. Acta Biomater. 2009;5(4):1035–45.
76. Kolan KC et al. Solvent and melt based extrusion 3D printing of polycaprolactone bioactive glass composite for tissue engineering. 2018.
77. Kolan K, et al. Solvent based 3D printing of biopolymer/bioactive glass composite and hydrogel for tissue engineering applications. Procedia CIRP. 2017;65:38–43.
78. El-Habashy SE, et al. Engineering 3D-printed core–shell hydrogel scaffolds reinforced with hybrid hydroxyapatite/polycaprolactone nanoparticles for in vivo bone regeneration. Biomaterials Sci. 2021;9(11):4019–39.
79. Ahn S, et al. Cells (MC3T3-E1)-laden alginate scaffolds fabricated by a modified solid-freeform fabrication process supplemented with an aerosol spraying. Biomacromolecules. 2012;13(9):2997–3003.
80. Yoon S, et al. Inkjet–spray hybrid printing for 3D freeform fabrication of multilayered hydrogel structures. Adv Healthc Mater. 2018;7(14):1800050.
81. Ozbolat IT, Hospodiuk M. Current advances and future perspectives in extrusion-based Bioprinting. Biomaterials. 2016;76:321–43.
82. Garakani SS, et al. Fabrication of Chitosan/polyvinylpyrrolidone hydrogel scaffolds containing PLGA microparticles loaded with dexamethasone for biomedical applications. Int J Biol Macromol. 2020;164:356–70.
83. Nooshabadi VT et al. Endometrial mesenchymal stem cell-derived exosome promote endothelial cell angiogenesis in a dose dependent manner: a new perspective on regenerative medicine and cell-free therapy. Archives Neurosci, 2019. 6(4).
84. Yu H, et al. Effects of 3-dimensional Bioprinting alginate/gelatin hydrogel scaffold extract on proliferation and differentiation of human dental pulp stem cells. J Endod. 2019;45(6):706–15.
85. Kazemi M, Dehghan MM, Azami M. Biological evaluation of porous nanocomposite scaffolds based on strontium substituted β-TCP and bioactive glass: an in vitro and in vivo study. Mater Sci Engineering: C. 2019;105:110071.
86. Kokubo T, Takadama H. How useful is SBF in predicting in vivo bone bioactivity? Biomaterials. 2006;27(15):2907–15.
87. Balmayor ER, et al. A novel enzymatically-mediated drug delivery carrier for bone tissue engineering applications: combining biodegradable starch-based microparticles and differentiation agents. J Mater Science: Mater Med. 2008;19:1617–23.

88. Derkach SR, et al. Interactions between gelatin and sodium alginate: UV and FTIR studies. Journal of Dispersion Science and Technology; 2019.
89. Sarker B, et al. Fabrication of alginate–gelatin crosslinked hydrogel microcapsules and evaluation of the microstructure and physico-chemical properties. J Mater Chem B. 2014;2(11):1470–82.
90. Wang Q-Q, et al. Alginate/gelatin blended hydrogel fibers cross-linked by Ca2 + and oxidized starch: Preparation and properties. Mater Sci Engineering: C. 2019;99:1469–76.
91. Goncalves EM, et al. Three-dimensional printed PCL-hydroxyapatite scaffolds filled with CNT s for bone cell growth stimulation. J Biomedical Mater Res Part B: Appl Biomaterials. 2016;104(6):1210–9.
92. Xu N, et al. 3D artificial bones for bone repair prepared by computed tomography-guided fused deposition modeling for bone repair. ACS Appl Mater Interfaces. 2014;6(17):14952–63.
93. Hassanajili S, et al. Preparation and characterization of PLA/PCL/HA composite scaffolds using indirect 3D printing for bone tissue engineering. Mater Sci Engineering: C. 2019;104:109960.
94. Tong SY, et al. Uniformly-dispersed nanohydroxapatite-reinforced Poly (ε-caprolactone) composite films for tendon tissue engineering application. Mater Sci Engineering: C. 2017;70:1149–55.
95. Bayer IS. Controlled drug release from nanoengineered polysaccharides. Pharmaceutics. 2023;15(5):1364.
96. Uskoković V. Mechanism of formation governs the mechanism of release of antibiotics from calcium phosphate nanopowders and cements in a drug-dependent manner. J Mater Chem B. 2019;7(25):3982–92.
97. Iurckevicz G et al. Encapsulated microparticles of (1→6)-β-d-Glucan containing extract of Baccharis dracunculifolia: production and characterization. Molecules, 2019. 24(11).
98. Adejuyigbe B, et al. Osteoporosis: molecular pathology, diagnostics, and therapeutics. Int J Mol Sci. 2023;24(19):14583.
99. Huang X, et al. Biomaterial scaffolds in maxillofacial bone tissue engineering: A review of recent advances. Bioactive Mater. 2024;33:129–56.
100. Ansari M. Bone tissue regeneration: biology, strategies and interface studies. Prog Biomater. 2019;8(4):223–37.
101. Wei H, et al. Recent advances in smart stimuli-responsive biomaterials for bone therapeutics and regeneration. Bone Res. 2022;10(1):17.
102. Bose S, Sarkar N, Jo Y. Natural medicine delivery from 3D printed bone substitutes. J Controlled Release. 2024;365:848–75.
103. Shi W, et al. Advancements in drug-loaded hydrogel systems for bone defect repair. Regenerative Therapy. 2024;25:174–85.
104. Nweke CE, Stegemann JP. Modular microcarrier technologies for cell-based bone regeneration. J Mater Chem B. 2020;8(18):3972–84.
105. Mohseni M, et al. Dexamethasone loaded injectable, self-healing hydrogel microspheresbased on UPy-functionalized Gelatin/ZnHAp physical network promotes bone regeneration. Int J Pharm. 2022;626:122196.
106. Noory P, et al. Human menstrual blood stem cell-derived granulosa cells participate in ovarian follicle formation in a rat model of premature ovarian failure in vivo. Cell Reprogramming. 2019;21(5):249–59.
107. Sharma N, Madan P, Lin S. Effect of process and formulation variables on the Preparation of parenteral paclitaxel-loaded biodegradable polymeric nanoparticles: A co-surfactant study. Asian J Pharm Sci. 2016;11(3):404–16.
108. Alex AT, et al. Development and evaluation of carboplatin-loaded PCL nanoparticles for intranasal delivery. Drug Delivery. 2016;23(7):2144–53.
109. Musumeci T, et al. PLA/PLGA nanoparticles for sustained release of docetaxel. Int J Pharm. 2006;325(1–2):172–9.
110. Feng S-s, Huang G. Effects of emulsifiers on the controlled release of Paclitaxel (Taxol®) from nanospheres of biodegradable polymers. J Controlled Release. 2001;71(1):53–69.
111. bt Ibrahim SF, Mohd Azam NAN, Mat KA, Amin. Sodium alginate film: The effect of crosslinker on physical and mechanical properties. In IOP Conference Series: Materials Science and Engineering. 2019. IOP Publishing.
112. Yang G, et al. Assessment of the characteristics and biocompatibility of gelatin sponge scaffolds prepared by various crosslinking methods. Sci Rep. 2018;8(1):1616.
113. Bigi A, et al. Mechanical and thermal properties of gelatin films at different degrees of glutaraldehyde crosslinking. Biomaterials. 2001;22(8):763–8.
114. Ji Yin Y, et al. Preparation and characterization of hydroxyapatite/chitosan–gelatin network composite. J Appl Polym Sci. 2000;77(13):2929–38.
115. Sharma C, et al. Fabrication and characterization of novel nano-biocomposite scaffold of chitosan–gelatin–alginate–hydroxyapatite for bone tissue engineering. Mater Sci Engineering: C. 2016;64:416–27.
116. Rajkumar M, et al. Nanohydroxyapatite–chitosan–gelatin polyelectrolyte complex with enhanced mechanical and bioactivity. Mater Sci Engineering: C. 2013;33(6):3237–44.
117. Hedayati SK, et al. Additive manufacture of PCL/nHA scaffolds reinforced with biodegradable continuous fibers: mechanical properties, in-vitro degradation profile, and cell study. Eur Polymer J. 2022;162:110876.
118. Affandi N, Ibrahim N, Fadil F. Tuning surface roughness of electrospun Poly Caprolactone fibres by single solvent electrospinning system. Digest J Nanomaterials Biostructures. 2020;15:1069–74.
119. Pan T, et al. 3D bioplotting of gelatin/alginate scaffolds for tissue engineering: influence of crosslinking degree and pore architecture on physicochemical properties. J Mater Sci Technol. 2016;32(9):889–900.
120. Negrini NC, et al. Tissue-mimicking gelatin scaffolds by alginate sacrificial templates for adipose tissue engineering. Acta Biomater. 2019;87:61–75.
121. Luo Y, et al. Concentrated gelatin/alginate composites for fabrication of predesigned scaffolds with a favorable cell response by 3D plotting. RSC Adv. 2015;5(54):43480–8.
122. Shi L, et al. Three-dimensional printing alginate/gelatin scaffolds as dermal substitutes for skin tissue engineering. Polym Eng Sci. 2018;58(10):1782–90.
123. Dorj B, et al. Robocasting nanocomposite scaffolds of Poly (caprolactone)/hydroxyapatite incorporating modified carbon nanotubes for hard tissue reconstruction. J Biomedical Mater Res Part A. 2013;101(6):1670–81.
124. Kolan KC et al. Bioprinting with human stem cell-laden alginate-gelatin Bioink and bioactive glass for tissue engineering. Int J Bioprinting, 2019. 5(2.2).
125. Murphy C et al. 3D printing of a polymer bioactive glass composite for bone repair. 2016.
126. Buyuksungur S, Hasirci V, Hasirci N. 3D printed hybrid bone constructs of PCL and dental pulp stem cells loaded GelMA. J Biomedical Mater Res Part A. 2021;109(12):2425–37.
127. Manoukian OS, et al. Spiral Layer-by-Layer Micro-Nanostructured scaffolds for bone tissue engineering. ACS Biomaterials Sci Eng. 2018;4(6):2181–92.
128. Borges J et al. Recent developments in Layer-by-Layer assembly for drug delivery and tissue engineering applications. Adv Healthc Mater. 2024;13:23027
129. Yang Y, et al. Highly elastic and ultratough hybrid ionic–covalent hydrogels with tunable structures and mechanics. Adv Mater. 2018;30(18):1707071.
130. Ren P, et al. Alginate/gelatin-based hybrid hydrogels with function of injecting and encapsulating cells in situ. Int J Biol Macromol. 2022;212:67–84.
131. Manaila E, Craciun G. Poly (acrylic acid)-Sodium alginate superabsorbent hydrogels synthesized by Electron-Beam Irradiation—Part II: swelling kinetics and absorption behavior in various swelling media. Gels. 2024;10(9):609.
132. Sittisanguanphan N, Paradee N, Sirivat A. Hyaluronic acid and graphene oxide-incorporated hyaluronic acid hydrogels for electrically stimulated release of anticancer Tamoxifen citrate. J Pharm Sci. 2022;111(6):1633–41.
133. Liu Q, et al. Formulation optimization and characterization of carvacrol-loaded nanoemulsions: in vitro antibacterial activity/mechanism and safety evaluation. Ind Crops Prod. 2022;181:114816.
134. Hong S-N, et al. Alleviation of surgery-induced osteitis in sinonasal cavity by dexamethasone-loaded Poly (lactic-co-glycolic acid)(PLGA) microparticles with strong calcium-binding affinity. Pharmaceutics. 2022;14(3):546.
135. Kim D-H, Martin DC. Sustained release of dexamethasone from hydrophilic matrices using PLGA nanoparticles for neural drug delivery. Biomaterials. 2006;27(15):3031–7.
136. Qi H, et al. Electrophoretic deposition of dexamethasone-loaded gelatin nanospheres/chitosan coating and its dual function in anti-inflammation and osteogenesis. Colloids Surf B. 2018;169:249–56.
137. Park M-H, Jang SJ, Choi SH. Osteogenic evaluation of hydroxyapatite scaffold loaded with dexamethasone In femoral drill holes. In vivo. 2020;34(4):1857–62.
138. Piao Z-G, et al. Osteogenic evaluation of collagen membrane containing drug-loaded polymeric microparticles in a rat calvarial defect model. Tissue Eng Part A. 2014;20(23–24):3322–31.
139. Zhang B, et al. Surface-decorated hydroxyapatite scaffold with on-demand delivery of dexamethasone and stromal cell derived factor-1 for enhanced osteogenesis. Mater Sci Engineering: C. 2018;89:355–70.
140. Kim SH, et al. Substance P/dexamethasone-encapsulated PLGA scaffold fabricated using supercritical fluid process for calvarial bone regeneration. J Tissue Eng Regen Med. 2017;11(12):3469–80.
141. Chen Y, et al. Promoted angiogenesis and osteogenesis by Dexamethasone-loaded calcium phosphate nanoparticles/collagen composite scaffolds with microgroove networks. Sci Rep. 2018;8(1):14143.

142. Chen Y, Kawazoe N, Chen G. Preparation of dexamethasone-loaded biphasic calcium phosphate nanoparticles/collagen porous composite scaffolds for bone tissue engineering. Acta Biomater. 2018;67:341–53.
143. Qiu K, et al. Electrophoretic deposition of dexamethasone-loaded mesoporous silica nanoparticles onto Poly (L-lactic acid)/poly (ε-caprolactone) composite scaffold for bone tissue engineering. ACS Appl Mater Interfaces. 2016;8(6):4137–48.
144. Asl MA, et al. Polyhydroxybutyrate-starch/carbon nanotube electrospun nanocomposite: A highly potential scaffold for bone tissue engineering applications. Int J Biol Macromol. 2022;223:524–42.
145. Preeth DR, et al. Bioactive zinc (II) complex incorporated PCL/gelatin electrospun nanofiber enhanced bone tissue regeneration. Eur J Pharm Sci. 2021;160:105768.
146. Hu J, et al. Vanillin-bioglass cross-linked 3D porous Chitosan scaffolds with strong osteopromotive and antibacterial abilities for bone tissue engineering. Carbohydr Polym. 2021;271:118440.
147. Wang CX, et al. Dopamine D1 receptor-mediated activation of the ERK signaling pathway is involved in the osteogenic differentiation of bone mesenchymal stem cells. Stem Cell Res Ther. 2020;11(1):12.
148. Wu M, Chen G, Li Y-P. TGF-β and BMP signaling in osteoblast, skeletal development, and bone formation, homeostasis and disease. Bone Res. 2016;4(1):1–21.
149. Komori T. Bone development by Hedgehog and Wnt signaling, Runx2, and Sp7. J Bone Miner Metab. 2024;43:1–6.
150. Yuasa M, et al. Dexamethasone enhances osteogenic differentiation of bone marrow-and muscle-derived stromal cells and augments ectopic bone formation induced by bone morphogenetic protein-2. PLoS ONE. 2015;10(2):e0116462.
151. Toledano M, et al. Dexamethasone-doped nanoparticles improve mineralization, crystallinity and collagen structure of human dentin. J Dent. 2023;130:104447.
152. Ma X, et al. Dexamethasone induces osteogenesis via regulation of Hedgehog signalling molecules in rat mesenchymal stem cells. Int Orthop. 2013;37:1399–404.
153. Zhang X, et al. Osteoblast derived extracellular vesicles induced by dexamethasone: A novel biomimetic tool for enhancing osteogenesis in vitro. Front Bioeng Biotechnol. 2023;11:1160703.
154. McLeod CM, Mauck RL. On the origin and impact of mesenchymal stem cell heterogeneity: new insights and emerging tools for single cell analysis. Eur Cell Mater. 2017;34:217–31.
155. Włodarczyk-Biegun MK. Del Campo, *3D Bioprinting of structural proteins*. Biomaterials. 2017;134:180–201.
156. Kochhar D, DeBari MK, Abbott RD. The materiobiology of silk: exploring the biophysical influence of silk biomaterials on directing cellular behaviors. Front Bioeng Biotechnol. 2021;9:697981.
157. Rezania N, et al. Three-dimensional printing of Polycaprolactone/hydroxyapatite bone tissue engineering scaffolds mechanical properties and biological behavior. J Mater Science: Mater Med. 2022;33(3):31.
158. Park J, et al. Three dimensional cell printing with sulfated alginate for improved bone morphogenetic protein-2 delivery and osteogenesis in bone tissue engineering. Carbohydr Polym. 2018;196:217–24.
159. Purohit SD, et al. Gelatin—alginate—cerium oxide nanocomposite scaffold for bone regeneration. Mater Sci Engineering: C. 2020;116:111111.
160. Amir LR, et al. Chitosan as a potential osteogenic factor compared with dexamethasone in cultured macaque dental pulp stromal cells. Cell Tissue Res. 2014;358:407–15.
161. Amjadian S, et al. The synergistic effect of nano-hydroxyapatite and dexamethasone in the fibrous delivery system of gelatin and Poly (l-lactide) on the osteogenesis of mesenchymal stem cells. Int J Pharm. 2016;507(1–2):1–11.
162. Zhou J, et al. Improving osteogenesis of three-dimensional porous scaffold based on mineralized Recombinant human-like collagen via mussel-inspired polydopamine and effective immobilization of BMP-2-derived peptide. Colloids Surf B. 2017;152:124–32.
163. Li Z, et al. Feeder-free self-renewal of human embryonic stem cells in 3D porous natural polymer scaffolds. Biomaterials. 2010;31(3):404–12.
164. Ivanovski S, et al. 3D printing for bone regeneration: challenges and opportunities for achieving predictability. Periodontol 2000. 2023;93(1):358–84.
165. Oladapo B, et al. 3D-printed biomimetic bone implant polymeric composite scaffolds. Int J Adv Manuf Technol. 2023;126(9):4259–67.
166. Pan P, et al. Biologically enhanced 3D printed micro-nano hybrid scaffolds doped with abalone shell for bone regeneration. Adv Compos Hybrid Mater. 2022;6(1):10.
167. Remy MT, et al. MicroRNA-200c release from Gelatin-Coated 3D-Printed PCL scaffolds enhances bone regeneration. ACS Biomaterials Sci Eng. 2024;10(4):2337–50.

Publisher's note